Stem Cell Research & Therapy

RESEARCH

Open Access

CircSPG21 ameliorates oxidative stress-induced senescence in nucleus pulposus-derived mesenchymal stem cells and mitigates intervertebral disc degeneration through the miR-217/SIRT1 axis and mitophagy

Yongbo Zhang[1,2†], Sheng Yang[1,2†], Xuan You[3,4†], Zhengguang Li[5], Liuyang chen[3,4], Rui Dai[3,4], Hua Sun[3,4] and Liang Zhang[3,4,5*]

Abstract

Background The microenvironment of intervertebral disc degeneration (IVDD) is characterized by oxidative stress, leading to the senescence of nucleus pulposus-derived mesenchymal stem cells (NPMSCs). The purpose of this study was to investigate the competitive endogenous RNA mechanism involved in the senescence of NPMSCs induced by tert-butyl hydroperoxide (TBHP).

Methods Bioinformatic analysis identified differentially expressed circRNAs. Interactions among circSPG21, miR-217, and the NAD-dependent protein deacetylase sirtuin-1 (SIRT1) were validated through dual-luciferase assays, RNA fluorescence in situ hybridization and RNA immune precipitation. β-Gal staining, EdU staining, Western blotting, JC-1 assays, cell cycle analysis, and quantitative reverse transcription PCR (RT—qPCR) were used to examine the functions of these molecules in TBHP-induced senescent NPMSCs. The therapeutic effects of circSPG21 were evaluated in a rat IVDD model.

Results CircSPG21 expression was significantly decreased in both human and rat IVDD tissues, whereas miR-217 was upregulated and SIRT1 was downregulated. Overexpression of circSPG21 alleviated NPMSC senescence by reducing P21 and P53 levels and restoring mitophagy through Parkin. The protective effects of circSPG21 were mediated through the miR-217/SIRT1 axis, as SIRT1 knockdown attenuated these benefits. CircSPG21 also ameliorated disc degeneration in the IVDD rat model, highlighting its potential as a therapeutic target.

Conclusion CircSPG21 reduces oxidative stress-induced NPMSC senescence through the miR-217/SIRT1 axis and mitophagy, providing new insights into IVDD and identifying circSPG21 as a potential therapeutic target for disc degeneration.

†Yongbo Zhang, Sheng Yang and Xuan You have contributed equally to this manuscript and shared the first authorship.

*Correspondence:
Liang Zhang
zhangliang6320@sina.com
Full list of author information is available at the end of the article

Keywords ceRNA, Nucleus pulposus-derived mesenchymal stem cell, Senescence, Mitophagy, Intervertebral disc degeneration

Background

Over the past thirty years, low back pain (LBP) has emerged as the leading cause of disability worldwide, with an increasing incidence rate that imposes a major economic burden on society and families [1]. Intervertebral disc degeneration (IVDD) is the primary cause of LBP; however, its pathogenic mechanisms remain unclear, and effective treatments are lacking. Existing treatment methods, including drug therapy or surgery, such as posterior lumbar interbody fusion (PLIF), merely relieve symptoms and fail to restore the structure and function of the intervertebral disc (IVD) [2].

In recent years, mesenchymal stem cells (MSCs), including adipose-derived MSCs, bone marrow-derived MSCs, and umbilical cord-derived MSCs, have been extensively applied in the treatment of degenerative disc diseases [3–5]. However, the microenvironment of IVDD is unsuitable for the survival of exogenous MSCs [6, 7]. In 2007, NPMSCs were first discovered in the nucleus pulposus (NP) tissue of human degenerative IVD, providing a new direction for the etiological study of IVDD [8]. Compared with exogenous stem cells, NPMSCs are more capable of adapting to the hypoxic and hyperosmotic microenvironments of degenerative IVD [6, 7, 9]. Thus, the use of NPMSCs is expected to become a novel strategy for treating IVDD.

In the past, it was believed that apoptosis, impaired mitophagy and senescence of NP cells (NPCs) were the main causes of IVDD, but research on the mechanisms involved in the relationship between NPMSCs and IVDD has been lacking [10–12]. The endogenous repair ability of degenerative IVDs is achieved by the differentiation of NPMSCs into NPCs [9]. With IVDD progression, the number of endogenous NPMSCs decreases gradually [13, 14]. NPMSCs derived from human degenerative IVD exhibit decreased cell proliferation and multilineage differentiation, decreased stem cell phenotypic expression, cell cycle arrest and increased apoptosis, indicating that the regenerative potential of NPMSCs decreases with increasing IVDD [15]. Our previous study revealed that NPMSCs derived from degenerative IVD of rats presented biological characteristics of cell senescence, such as weakened cell proliferation, decreased stemness maintenance and increased cell apoptosis [7]. In addition, pathological factors such as oxidative stress and annulus fibrosus (AF) rupture can trigger the senescence and apoptosis of nuclear NPMSCs, ultimately resulting in irreversible IVDD [16, 17]. After simulating the degenerative microenvironment with H_2O_2, we found that NPMSCs presented obvious characteristics of cell senescence, such as slower cell proliferation, increased β-galactosidase (β-gal) activity and upregulated expression of senescence-related proteins (P16, P21 and p53) [18, 19]. The local accumulation of senescent MSCs can increase the expression of components associated with the senescence-associated secretory phenotypes (SASPs),) such as IL-1β, IL-6 and IL-8, which may induce the senescence of local normal cells and stem cells [20]. In our preliminary study, urolithin A alleviated oxidative stress-induced NPMSCs senescence and mitigated IVDD progression in a rat model [19]. In follow-up research, we discovered that mitochondrial dysfunction in senescent NPMSCs and that promoting mitochondrial function can mitigate NPMSCs senescence induced by oxidative stress [21]. Consequently, the decreased quantity, impaired function, and senescence of endogenous NPMSCs could be a primary cause of challenges in the endogenous repair of IVDD. However, the specific mechanisms underlying NPMSCs senescence and mitochondrial function remain unclear, underscoring the need for further investigation.

CircRNAs feature a closed circular structure without 5' and 3' ends, making them resistant to degradation by nucleases such as RNase, and this structure significantly increases circRNA stability in both cellular and vitro environments, resulting in a longer half-life than that of linear RNAs (e.g., mRNAs), thereby extending their functional duration in the body [22, 23]. CircRNAs contain many microRNA (miRNA) response elements, which can function as molecular sponges of miRNAs to regulate the expression of target genes. This characteristic allows circRNAs to regulate the expression of target genes by acting as competitive endogenous RNAs (ceRNAs) at the post-transcriptional level [23]. Extensive studies have shown that circRNAs play important roles in a variety of pathological processes, including regulating cell senescence and mitophagy through ceRNAs in degenerative diseases [24, 25]. Therefore, circRNAs hold promise as a treatment for various diseases, but studies on circRNAs in NPMSCs are still limited.

Increasing evidence reveals the role of ceRNAs in the pathogenesis of IVDD. Our previous study revealed that circRNA-VMA21 could regulate NPCs apoptosis by acting as a ceRNA of miRNA-200c and delaying

IVDD in vivo [26]. The overexpression of circERCC2 can inhibit NPCs apoptosis, whereas an NAD-dependent protein deacetylase sirtuin-1 (SIRT1) inhibitor can block the protective effect of circERCC2 on NPCs apoptosis and mitophagy, which suggested that circERCC2 can inhibit NPCs apoptosis through the miRNA-182-5p/SIRT1 axis [27]. CircFOXP1 is abundant and stable in the cytoplasm of MSCs and acts as a ceRNA of miRNA-17-3p and miRNA-127-5p, promoting cell proliferation and differentiation [28]. In addition, circSERPINE2 silencing restrains MSCs senescence via the YBX3/PCNA/p21 axis [29]. Therefore, circRNAs could act as ceRNAs of miRNAs to regulate the proliferation and differentiation of MSCs and to regulate MSCs senescence. However, the role of circRNAs in NPMSCs senescence and mitochondrial function remains unclear. Therefore, research on the senescence mechanism of endogenous NPMSCs will help reveal a new pathological mechanism of IVDD and provide a theoretical basis for the treatment of IVDD-related diseases.

In this study, tert-butyl hydroperoxide (TBHP), which is widely used to generate an in-vitro-model of senescence, was used to trigger oxidative stress in NPMSCs. CircSPG21 (hsa_circ_0003526 in circBase) was selected based on bioinformatic analysis, and its role through the miR-217/SIRT1 axis in the regulation of NPMSCs senescence and puncture-induced IVDD in a rat model was explored. This is the first study of circRNA in NPMSCs, and regulating circRNA expression in NPMSCs may be a potential treatment for IVDD.

Methods

Human NP tissue collection

Human NP tissues were collected from 15 patients who underwent PLIF due to IVDD or trauma, with 6 normal and 9 IVDD samples utilized for NPMSCs isolation and correlation analysis of circSPG21, miR-217 and SIRT1 expression and Pfirrmann grades through quantitative reverse transcription (RT-qPCR) analyses. The magnetic resonance imaging (MRI) grade is a 5-point grading system according to the Pfirrmann grade, and grades I-II indicate normal tissue, whereas grades numerals III-V indicate degenerated tissue [30]. The line regression plots were analyzed via regression plot tools in Hiplot Pro (https://hiplot.com.cn/), a comprehensive web service for biomedical data analysis and visualization [31]. All human-related tissues included in this study were approved by the Ethics Committee of Northern Jiangsu People's Hospital (2021ky050). Patient information is included in Supplementary Table 1 (Table S1).

Bioinformatic analysis of circRNAs

CircRNA microarray expression profiles were generated from normal and degenerative NP tissues. The dataset GSE67566 was obtained from the GEO (https://www.ncbi.nlm.nih.gov/geo/) database to identify differentially expressed circRNAs [32] (Table S2). R (version 4.2.2) was used to identify differentially expressed circRNAs among groups via using the "Limma" R package. Specifically, volcano plots revealed the differentially expressed circRNAs whose expression was downregulated or upregulated. Heatmaps representing the differentially expressed circRNAs across all the samples were generated via the R package "heatmap". The predicted targets of circSPG21 were analysed via the cancer-specific circRNA database (CSCD, http://geneyun.net/CSCD2) [33] and CircInteractome tool (bin/circsearchTest) [34], in which miR-217 was predicted. The target genes of miR-217 were predicted via various programs, including TargetScan (https://www.targetscan.org/vert_80) [35], RtarBase (https://mirtarbase.cuhk.edu.cn/) [36], and miRecords (http://mirecords.umn.edu/miRecords) [37].

RT–qPCR

RT-qPCR was used to detect the expression levels of RNA in different samples [38, 39]. Total RNA from NP tissue and NPMSCs was extracted via TRIzol reagent (Invitrogen, USA) and reverse transcribed via the HiScript III 1st Strand cDNA Synthesis Kit (+gDNA wiper) (Vazyme Biotech, China). The primer sequences used were designed and synthesized by Sangon Biotech (Table 1). Amplification of the cDNA was performed via Taq Pro Universal SYBR qPCR Master Mix (Vazyme Biotech, China) according to the manufacturer's instructions. The expression levels of the target genes were calculated via the 2-ΔΔCt method. The expression levels of the circRNAs and mRNAs were normalized to GAPDH, whereas those of the miRNAs to U6.

Isolation and culture of NPMSCs

All animal-related operations involved in this study were approved by the Animal Ethics Committee of Yangzhou University (202,103,427). Sprague–Dawley (SD) rats were purchased from the Comparative Medical Center of Yangzhou University [Licence No. SCXK (Su) 2022–0009]. The method for NPMSCs extraction and separation was performed as previously described [39, 40]. NP tissue from SD rat tail IVD was isolated under aseptic procedures, finely minced appropriately, placed in complete medium containing 0.2% collagenase type II (Gibco, USA) and digested in a 37 °C, 5% CO_2 incubator for 12 h. After digestion, the obtained cells and some incompletely digested tissues were washed twice

Table 1 Primer sequence summary

Gene	Primer sequence-forward	Primer sequence-reverse
hsa_circ_0003526	GCAATTCCTTCAGTGACACCT	GGGAACTGTACCTCTAAACCAGT
hsa_circ_0082686	CACACTTCATCCTCACCACTGA	CCTCCCATTTGCCTCTATCCAA
hsa_circ_0036763	CAGAGAAGAAACAGCAGTGCAG	TGGAGATGTGTTCAGCTTCGAA
hsa_circ_0003258	AGTTCATGTGCCAGTGGTGT	TCCAGAATGCTGCAAGGAGT
hsa_circ_0003183	CGCCAGCATTCCAATTCCAA	ACGACCTTGTGATGGAACGA
hsa_circ_0072464	CATCAAGACAAGCCAGCAGC	CGGATGTTATCAGCCCCTCC
hsa_circ_0037896	TCCTGGGAAAGCTGGAATCAG	AATTGGCAGCCTGATTGGTCC
hsa_circ_0075071	TGTTCCCTTTGCTGCCGTAG	TGCTTTGATCCCATCGAGGTT
hsa_circ_0032254	GGTGGCTAGAAGACATCGCA	AGGAGTAGTGCTGAGGGAGG
hsa_circ_0001345	TGCGTAGATGTGCTTGGGAGAAATG	AACACAATGTGCATTCACAGCCAAC
h-miR-217	AGCGAGGCTACTGCATCAGGA	ATCCAGTGCAGGGTCCGAGG
h-SIRT1	TAGCCTTGTCAGATAAGGAAGGA	ACAGCTTCACAGTCAACTTTGT
h-PPM1D	CTGTACTCGCTGGGAGTGAG	GTTCGGGCTCCACAACGATT
h-KRAS	ACAGAGAGTGGAGGATGCTTT	GCCTGTTTTGTGTCTACTGTTCT
h-DACH1	GGGGCTTGCATACGGTCTAC	CGAACTTGTTCCACATTGCACA
h-U6	CTCGCTTCGGCAGCACATATACT	CTCGCTTCGGCAGCACATATACT
h-GAPDH	GGAGCGAGATCCCTCCAAAAT	GGCTGTTGTCATACTTCTCATGG
r-circSPG21	ATGGACTGCAAACAGGGTTAAC	CCAGCATCATAGAGTGACCAGAT
r-miR-217	CTGGGTCGTATCCAGTGCAA	GTCGTATCCAGTGCGTGTCG
r-SIRT1	TGACCTCCTCATTGTTATTGGG	GGCATACTCGCCACCTAACCT
r-U6	CTCGCTTCGGCAGCACA	AACGCTTCACGAATTTGCGT
r-GAPDH	CTGGAGAAACCTGCCAAGTATG	GGTGGAAGAATGGGAGTTGCT

with phosphate-buffered saline (PBS), filtered through a 75 μm pore size filter, and centrifuged at 1000 r/minute for 5 min. Then, the obtained cells were transferred to complete MSCs medium and cultured at 37 °C in a 5% CO_2 incubator. The culture medium was changed every 2 days. The cells were passaged at a 1:3 ratio when they reached 80% to 90% confluence. The cells at passage 3 were frozen for subsequent experiments.

Surface marker identification of NPMSCs

Immunofluorescence staining was used to assess the surface markers of the NPMSCs [39, 40]. Cell slides 20 mm in diameter pretreated with polylysine were placed in 12-well plates. NPMSCs were added to complete MSCs medium and mixed with gentle shaking. The appropriate amount of cell suspension was then added to the 12-well plate and incubated at 37 °C in a 5% CO_2 incubator. After the cells were adherent and stable, the medium was removed, the cells were washed twice with PBS, fixed with 4% paraformaldehyde for 30 min, washed twice with PBS containing 0.5% Triton X-100 (15 min each time), and blocked with 10% bovine serum albumin for 1 h at room temperature. The slides were then incubated overnight at 4 °C with the following primary antibody solutions: anti-CD105 (Proteintech, China), anti-CD90 (ABclonal, China), anti-CD73 (ABclonal, China), anti-CD45 (ABclonal, China), anti-CD34 (ABclonal, China) and anti-Tie2 (Biodragon, China) (1:100). The cell slides were washed 3 times (5 min each time) with PBS, incubated with FITC (Proteintech, China)- or TRITC (Proteintech, China) (1:500)-labelled secondary antibody solution at room temperature in the dark for 1 h, washed 3 times (5 min each time) with PBS, and incubated with 4',6-diamidino-2'-phenylindole (DAPI) solution containing antifluorescence quenching sealing solution at room temperature in the dark for 10 min. Then, the slides were observed and photographed under a fluorescence microscope (Zeiss, Germany). The fluorescence intensity was analyzed via ImageJ software.

Multilineage differentiation

For verification of the multidirectional differentiation potential of the NPMSCs, osteogenic, adipogenic and chondrogenic differentiation was induced [39, 40]. NPMSCs were seeded in 6-well plates and cultured to approximately 70%, 100%, and 100% confluence. The medium was subsequently replaced with osteogenic, chondrogenic, or adipogenic differentiation medium (Cyagen, China), and the medium was changed regularly according to the manufacturer's instructions. After the induction period, the medium was removed, and the cells were washed three times with PBS, fixed with

4% paraformaldehyde for 30 min, and then treated with Alizarin Red, Alcian blue, or Oil Red O. At the end of the treatment, the cells were washed three times with PBS. Finally, the sections were observed and photographed under an inverted microscope.

Cell viability assay

For identification of a suitable TBHP concentration to establish an oxidative stress-induced senescence model of NPMSCs [19, 41], a Cell Counting Kit-8 (CCK-8, Beyotime, China) assay was used to evaluate cell viability [42]. An appropriate amount of NPMSCs was added to the MSCs complete medium and gently shaken to achieve a cell density of 2×10^4/mL. One hundred microlitres of cell suspension was taken from each well and added to a 96-well plate. The cells were cultured at 37 °C in a 5% CO_2 incubator overnight to ensure that the cells adhered to the plate stably. The cells were subsequently treated with various concentrations of TBHP (0, 20, 50, 100, 150, and 200 μM) for different durations (0, 6, 12, 24, and 48 h). After TBHP treatment, a CCK-8 assay was used to determine cell viability in different treatment groups according to the manufacturer's instructions. The optical density (OD) values were read at 450 nm via a microplate reader (Bio-Rad, USA). The cell viability was calculated as follows: cell viability (of control) = [(Ae-Ab)/(Ac-Ab)]. Ae, Ab, and Ac represent the OD values of the TBHP treatment, blank and control groups, respectively.

Cell proliferation assay

A 5-ethynyl-2'-deoxyuridine (EdU) cell proliferation kit with Alexa Fluor 488 (Beyotime, China) was used to evaluate the cell proliferative capacity of the NPMSCs [43]. NPMSCs (5×10^4 cells/well) were seeded in a 6-well plate and cultured in a 37 °C and 5% CO_2 incubator. When stably adhered to the plate, the cells in the different groups were treated according to the manufacturer's instructions. After incubation with EdU for 2 h, the NPMSCs were fixed with 4% paraformaldehyde for 15 min at room temperature, washed three times (5 min each time) with PBS, permeabilized with 0.5% Triton X-100 for 15 min, and washed twice (5 min each time) with PBS. The cells were subsequently incubated for 30 min at room temperature in the dark with click additive solution. The cells were then washed three times (5 min each time) with PBS and incubated with Hoechst 33,342 in the dark at room temperature for 10 min. Six random microscopic fields were subsequently observed and paragraphed under a fluorescence microscope and analyzed via ImageJ software.

Senescence-associated β-galactosidase (SA-β-Gal) staining

A SA-β-Gal staining kit (Beyotime, China) was used to evaluate the SA-β-Gal activity of the NPMSCs [44]. NPMSCs were seeded in a 6-well plate at a density of 4×10^4 cells/well and incubated at 37 °C with 5% CO_2 overnight. The cells were then treated following the manufacturer's instructions after treatment. In brief, the cell culture medium was removed, the cells were washed with PBS twice (5 min each), SA-β-Gal fixative was added, and the cells were fixed for 15 min. After the samples were washed with PBS twice (5 min each time), SA-β-Gal staining solution was added, the samples were sealed with plastic wrap, and they were incubated at 37 °C without CO_2 overnight. Six random microscopic fields were observed via fluorescence microscopy and then analysed via ImageJ software.

Cell transfection

The plasmid was designed by Shanghai Genechem. NPMSCs (5×10^5 cells/well) were seeded in 6-well plates and transfected with circSPG21, circSPG21-mut, miR-217-inhibitor, NC-inhibitor, SIRT1-shRNA and NC-shRNA via the Lipofectamine 3000 Transfection Kit (Thermo, USA) according to the manufacturer's instructions [45]. Briefly, cells were first seeded at 70–90%. Lipofectamine 3000 Reagent was diluted in Opti-MEM (Thermo, USA) and mixed well. The Prepare master mixture of the plasmid was prepared by diluting the plasmid in Opti-MEM, after which P3000 Reagent was added. The diluted plasmid was added to diluted Lipofectamine 3000 Reagent (1:1 ratio). The mixture was incubated for 10–15 min at room temperature, after which the plasmid–lipid complex was added to the cells. After 12 h of transfection, the medium was replaced with fresh complete medium, and the NPMSCs were cultured for an additional 24 h before being harvested for further experiments.

Cell cycle assay

The cell cycle phases of the NPMSCs were determined via flow cytometric analyses with a Cell Cycle Detection Kit (Keygen, China) [21]. NPMSCs from each group were collected from a 6-well plate and treated according to the manufacturer's instructions. The cells were collected by washing with PBS, the cell concentration was adjusted to 1×10^6 cells/mL, the cell suspension was centrifuged, the supernatant was discarded, and 70% cold ethanol was added overnight for fixation at 4 °C. The fixative was washed away with PBS, the staining solution was added, and the samples were incubated in the dark at room temperature for 60 min. The cell cycle phases were then measured via flow cytometry (BD Company, USA) [46].

JC-1 assay for determining the mitochondrial membrane potential (MMP)

The MMP of NPMSCs in the different groups of 6-well plates was determined via the use of the fluorescent probe iodide 5,5′,6,6′-tetrachloro-1,1′,3,3′-tetraethylbenzimidazolcarbocyanine (JC-1) detection kit (Beyotime, China) according to the manufacturer's instructions [19, 47]. After treatment, normal NPMSCs emit red fluorescence, and cells with damaged mitochondria emit green fluorescence. The culture medium was discarded, the cells were washed once with PBS, cell culture medium and JC-1 staining solution were added, and the mixture was mixed well. The cells were incubated in a cell incubator at 37 °C for 20 min. After incubation, the supernatant was removed, and the cells were washed twice with JC-1 staining buffer. Six random microscopic fields were observed by fluorescence microscopy to detect fluorescence and photograph. The ratio of green to red fluorescence intensity was analyzed via ImageJ software.

RNA fluorescence in situ hybridization (FISH)

Passage 3 NPMSCs were seeded on coverslips and used to perform FISH [48]. Blue fluorescence (DAPI), green fluorescence (TYR-488, Invitrogen, USA) and red fluorescence (TYR-651, Invitrogen, USA) indicated the nucleus, circSPG21 and miR-217, respectively. The samples were fixed with 4% paraformaldehyde for 30 min and then washed twice with PBS. The mixture was incubated with permeabilization solution for 15 min. The probe was prepared by dissolving it in hybridization buffer (Phenomenex, China) and applying it to the samples. The mixture was incubated at 37 °C for 4 h overnight. After hybridization, the cell coverslips were placed in 2 × Saline-Sodium Citrate (SSC; Phenomenex, China) solution and washed at 37 °C for 5 min. The mixture was transferred to 1 × SSC solution and washed again at 37 °C for 5 min, followed by a final wash in 0.2 × SSC at 37 °C for 5 min. After the cell nuclei were counterstained with DAPI, the slides were mounted with antifade mounting medium. The images were then acquired under a fluorescence microscope.

RNA immunoprecipitation (RIP) assay

RIP assays were performed via an RNA-binding protein immunoprecipitation kit (Millipore, USA) according to the manufacturer's instructions [49]. In brief, magnetic beads were first mixed with anti-Ago antibody or anti-IgG antibody (Abcam, USA), and then, the NPMSCs were dissolved in RNA lysis buffer. The lysates were then added to the beads, mixed and incubated overnight at 4 °C. After centrifugation, the supernatant was discarded, and the beads were rinsed twice with low-salt rinse solution (1 mmol/l $MgCl_2$, 0.05% NP40, 2 mmol/l EDTA, 1 mmol/l DTT, and 100 U/ml RNasin ribonidase inhibitor) and high-salt rinse solution (300 mmol/l NaCl) at 4 °C. Then, the beads were resuspended in Proteinase K solution and incubated at 55 °C for 10 min. The RNA was extracted via the TRIzol method and purified for further RT–qPCR analysis. Relative enrichment was normalized to the input.

Dual-luciferase reporter assay

The Dual-Luciferase reporter assay was used to determine the binding ability of circSPG21 to miR-217 and miR-217 to SIRT1[50]. The TargetScan Human database [35] (https://www.targetscan.org/vert_80/) was used to predict the complementary binding site of miR-217 in circSPG21 and miR-217 in the 3'-UTR of SIRT1 mRNA. The plasmid was designed by Shanghai Genechem.

(See figure on next page.)

Fig. 1 Analysis of circSPG21-miR-217-SIRT1 interactions in human and rat models of IVDD. **A** Volcano plot of differentially expressed circRNAs between normal and degenerative nucleus pulposus (NP) tissues, with significant upregulation and downregulation represented by red and blue dots, respectively. The vertical line corresponds to 2.0-fold upregulation between degenerative samples and controls, and the horizontal line represents an adjusted P value of 0.01. **B** Heatmap of differentially expressed circRNAs, highlighting circSPG21 (hsa_circ_0003526) prominently among the altered circRNAs. The red color indicates the degree of the upregulation in degenerated tissue while the green color indicates the degree of downregulation. RTarBase, miRecords, and TargetScan. **C** The result of the intersection of miRNAs (miR-217) predicted to bind with circSPG21 from CSCD and Interactome is displayed in the Venn diagram, revealing one intersecting miRNA. **D** The intersection of target genes (PPM1D, SIRT1, KRAS and DACH1) predicted to bind with miR-217 from RTarBase, miRecords, and TargetScan is displayed in the Venn diagram. **E** Predicted miRNA interaction network of circSPG21 based on CSCD and interactome analyses. All predicted miRNAs are displayed, with orange highlighting the circSPG21/miR-217/SIRT1 axis, which was further validated and investigated in this study. The top ten downregulated circRNAs in degenerative tissues and the four target genes are also shown. **F** Representative sagittal T2-weighted MRI images of human NP tissues displaying varying Pfirrmann grades (I-V), demonstrating different levels of disc degeneration. **G**–**I** The regression plots of the circSPG21 (**G**), miR-217 (**H**), and SIRT1 (**I**) expression levels in human NP tissues with different grades of degeneration, n = 3. The distribution of values is represented by the blue dots, and the trend line is represented by the blue line. **J** T2-weighted MRI and haematoxylin and eosin (HE, scale bar, 1 mm), stained histological images comparing the normal and IVDD groups of rats, confirming the establishment of the IVDD rat model. The data are expressed as the mean ± SD; *$P < 0.05$, **$P < 0.01$ indicates statistical significance, n = 6. **K**—**M** RT—qPCR analysis showing expression levels of circSPG21 (**K**), miR-217 (**L**), and SIRT1 (**M**) in the NP tissues from the control and IVDD group, with expression patterns mirroring those observed in human samples. The data are expressed as the mean ± SD; *$P < 0.05$, **$P < 0.01$ indicates statistical significance, n = 6

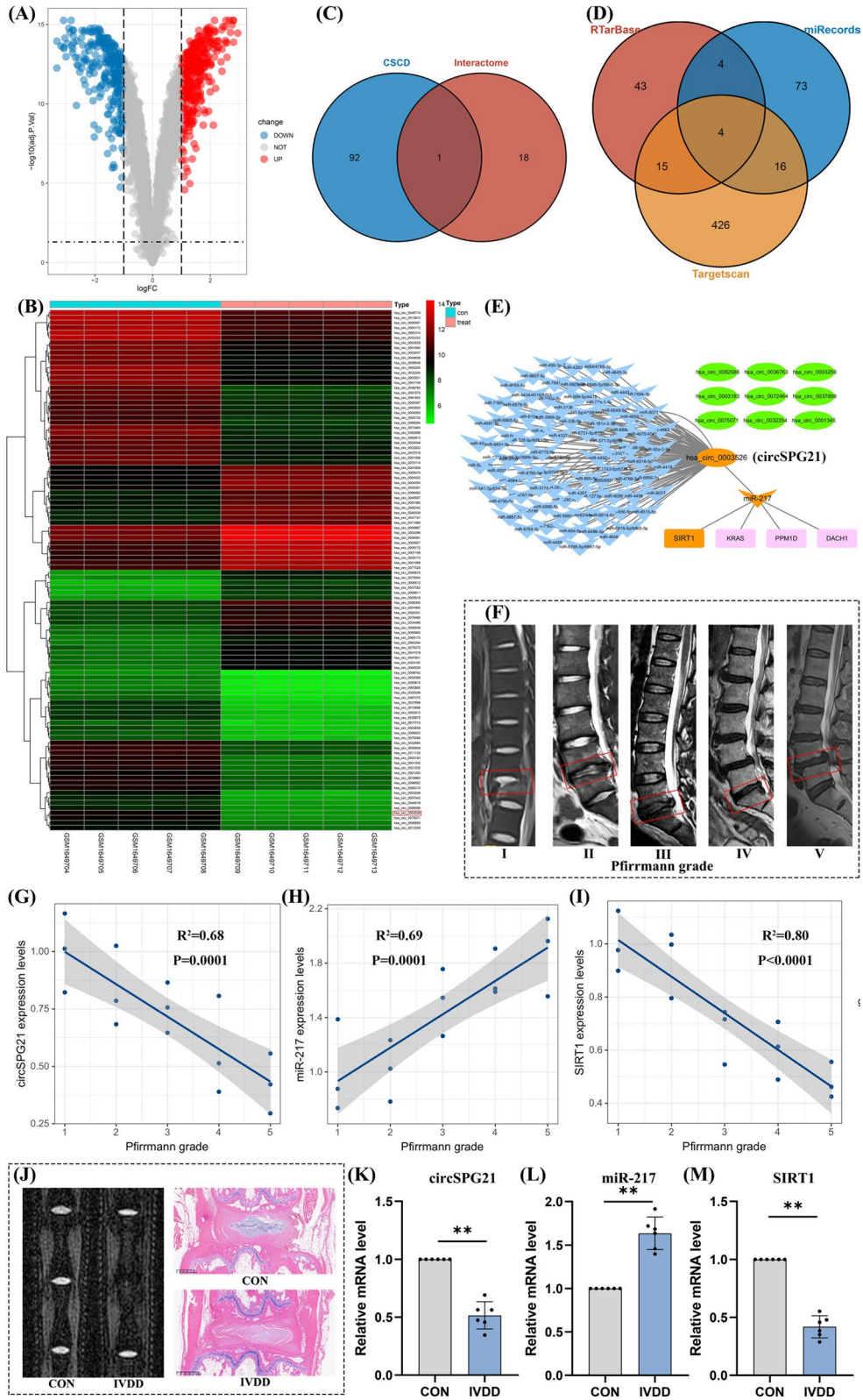

Fig. 1 (See legend on previous page.)

NPMSCs (1×10^5 cells/well) were seeded in 96-well plates and cotransfected with circSPG21, circSPG21-mutant (circSPG21-mut), miR-217, or SIRT1 3'-UTR wild-type plasmid or mutant plasmid with the miR-217-5p mimic or mimic control according to the Lipofectamine 3000 Transfection protocol. After 48 h, luciferase activity was measured with a dual-luciferase reporter assay kit (Beyotime, China) according to the manufacturer's instructions. The cell culture plate was removed and incubated at room temperature for 10 min. Dual-Lumi firefly luciferase assay reagent or Renilla luciferase assay reagent (100 μL per well) was added and mixed thoroughly. The mixture was incubated at room temperature for 10 min, after which a microplate reader was used for chemiluminescence detection.

Western blot analysis

Western blot analysis was used to detect the expression levels of proteins in different samples [51]. After different treatments, total cellular protein was extracted according to the manufacturer's instructions (Whole Cell Lysis Assay Kit, Keygen Biotech, China) and quantified via the BCA method (Enhanced BCA Protein Assay Kit, Beyotime, China). Equal amounts of protein samples (30–40 μg) from each group were separated via sodium dodecyl sulphate–polyacrylamide gel electrophoresis (SDS–PAGE). After electrophoresis, the proteins in the gel were transferred to polyvinylidene difluoride (PVDF) membranes in an ice bath. The membranes were then blocked with 5% skim milk for 2 h at room temperature. At the end of blocking, the membranes were then incubated overnight at 4 °C at the appropriate concentrations of primary antibody solution: GAPDH (1:1000; Servicebio, China), P21 (1:1000; Proteintech, China), P53 (1:5000; Abcam, UK), Parkin (1:1000; Proteintech, China), PTEN-induced putative kinase 1 (PINK1, 1:1000; Proteintech, China), and SIRT1 (1:1000; Abcam, UK). At the end of the incubation, the membranes were washed 3 times with 1 × TBST for 15 min each time on a shaker at room temperature and then incubated for one hour with horseradish peroxidase (HRP)-labelled secondary antibody solution (1:5000; Abcam, UK) on a shaker at room temperature. Afterwards, the membranes were washed another 3 times. Finally, an enhanced chemiluminescence system was used to obtain protein band images, and ImageJ software was used to analyse the relative expression of target proteins in each protein sample.

Rat IVDD model induction and lentivirus injection

The lentivirus with green fluorescent protein (GFP) was designed by Shanghai Genechem. The steps are simplified as follows [52, 53]. A linearized vector was obtained via using restriction enzyme digestion. The target gene fragment was prepared via RT-qPCR amplification. When the amplification primers are designed, homologous recombination sequences are added at the 5' end for target gene fragment amplification. The terminal sequences at the 5' and 3' ends of the amplification product exactly match those of the linearized cloning vector. A reaction system with the linearized vector and amplified gene product was created for the recombination reaction, achieving in vitro circularization of the vector and gene fragment. The recombination product was then transformed, and the correct bacterial clone was expanded and extracted to yield high-purity plasmids for downstream viral packaging. Validation of lentiviral expression in cells and NP tissue is shown in Fig. S1A.

Healthy rats (3–4 months old, weighing 300–400 g) were used for cell extraction and subsequent animal experiments. Twenty-four SD rats were randomly divided into four groups via a random number generator (n = 6 per group): the Con group (no operation), IVDD group (punctured), IVDD + circSPG21 group (punctured and injected with lentivirus circSPG21), and IVDD + circSPG21-mut group (punctured and injected with lentivirus circSPG21-mut). Briefly, the rats in the IVDD group, IVDD + circSPG21 group and IVDD + circSPG21-mut group were anaesthetized via an intraperitoneal injection

(See figure on next page.)

Fig. 2 Characterization of NPMSCs and establishment of the TBHP-induced cell senescence model. **A** Measurements of surface markers (CD73, CD90, CD105 and Tie2) detected by fluorescence staining and differentiation assays (osteogenic, adipogenic, and chondrogenic) of NPMSCs. Green fluorescence indicates CD34, CD45, and CD73, while red fluorescence indicates CD90, CD105, CD73, and Tie2 (scale bar, 250 μm). Alizarin Red, Oil Red O, and Alcian blue staining were positive after induced differentiation of NPMSCs (scale bar, 250 μm). **B** CCK-8 assays of NPMSCs treated with varying concentrations of TBHP (0, 20, 50, 100, 150, and 200 μM) for different durations (0, 6, 12, 24, and 48 h). The data are expressed as the mean ± SD; *$P < 0.05$, **$P < 0.01$ indicates statistical significance, n = 6. **C** SA-β-Gal staining of NPMSCs in the control group and TBHP group (scale bar, 250 μm). Senescent cells exhibit blue-stained high expression of SA-β-Gal. **D** EdU assays of NPMSCs of different groups (scale bar, 250 μm). Green fluorescence represents cells in a proliferating state, and blue fluorescence represents cell nuclei. **E** Quantitative analysis of the SA-β-Gal staining results. The data are expressed as the mean ± SD; *$P < 0.05$, **$P < 0.01$ indicates statistical significance, n = 6. **F** Quantitative analysis of the EdU results. The data are expressed as the mean ± SD; *$P < 0.05$, **$P < 0.01$ indicates statistical significance, n = 6. **G**–**I** RT–qPCR of circSPG21 (**G**), miR-217 (**H**), and SIRT1 (**I**) levels in NPMSCs in the different groups. The data are expressed as the mean ± SD; *$P < 0.05$, **$P < 0.01$ indicates statistical significance, n = 6. (J): Flow diagram presenting the main plan and process of the cell experiments

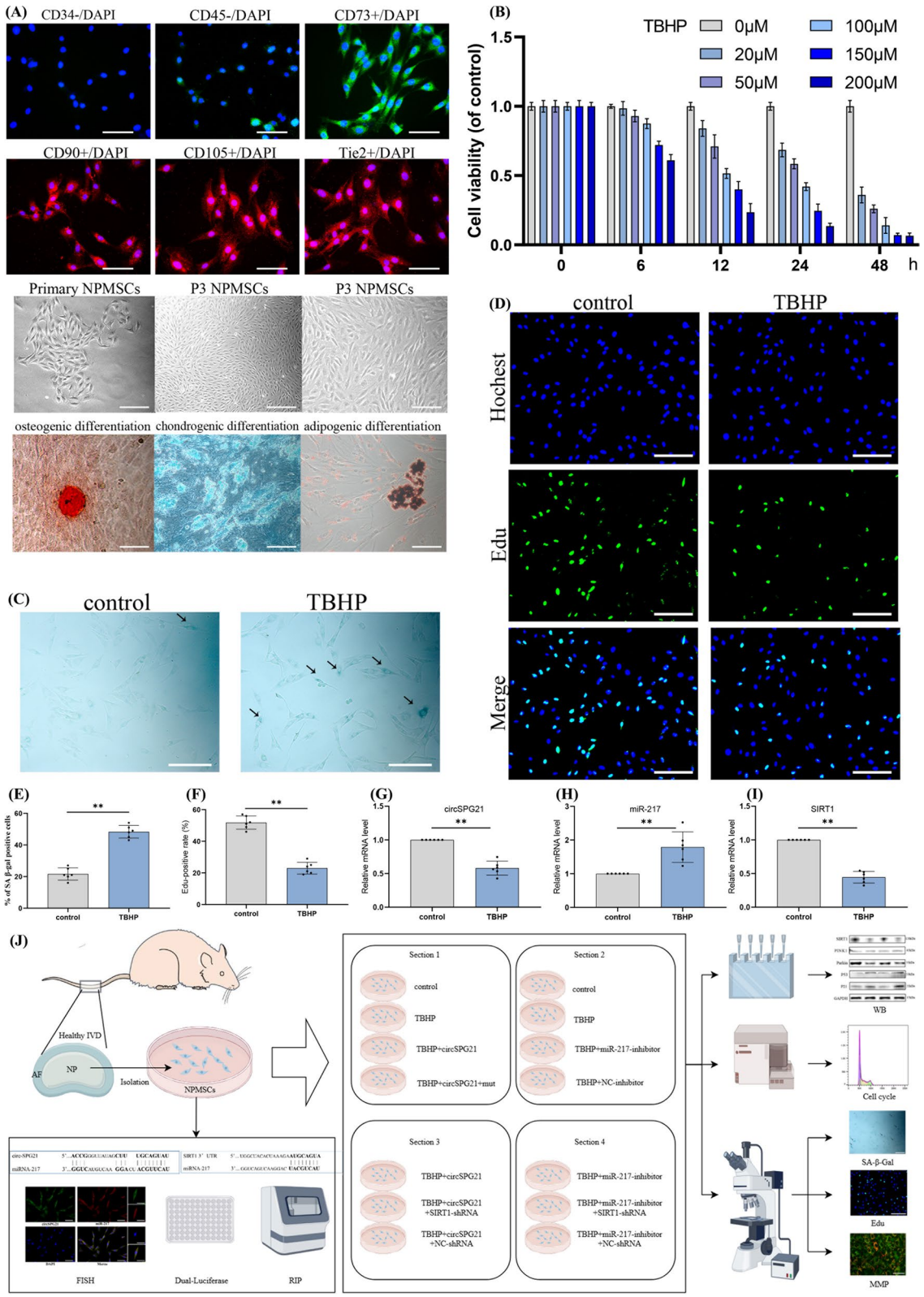

Fig. 2 (See legend on previous page.)

of 0.1 mg/kg pentobarbital sodium and placed in the prone position. The target disc (Co 6–7) was positioned and marked, the puncture site was sterilized, and the target disc was percutaneously punctured with a 21G fine needle under sterile conditions (puncture depth of 5 mm, rotated 180° after insertion, and held in place for 5 s) [54]. Two weeks after the puncture, 2 μl of lentivirus circSPG21 (1E + 8TU/mL) or lentivirus circSPG21-mut (1E + 8TU/mL) was injected into the puncture disc in the IVDD + circSPG21 group or the IVDD + circSPG21-mut group, respectively, via a 31G fine needle.

Imaging evaluation and histological analysis

Before modelling and 4 weeks after lentivirus injection, the rats were anaesthetized with pentobarbital sodium, after which X-rays and MR images of the caudal vertebrae were taken. The disc height index (DHI) and Pfirrmann grade of IVDD were calculated according to methods reported previously [55]. After the last imaging examination, the rats were sacrificed with an overdose of pentobarbital sodium, and the tails were harvested. The specimens were fixed in 10% neutral formalin fixative for 48 h, decalcified in EDTA decalcification solution for 1 month, dehydrated with gradient alcohol, and finally embedded in paraffin. The samples were sectioned into 5 μm thick slices, which were subsequently stained with haematoxylin–eosin (HE) and safranin O-fast green in accordance with the manufacturer's instructions. Histological scoring was performed as described previously [56]. This histologic score ranges from 3 to 15. Higher scores indicate more severe degeneration.

Statistical analysis

The data were expressed as the means ± SDs. Data analysis was performed with GraphPad Prism 8 (GraphPad, La Jolla). Differences between two groups were tested for statistical significance via using Student's t test, whereas multiple independent groups were tested via one-way analysis of variance (ANOVA). The Kruskal–Wallis H test was used to analyse the histological scores. The quantitative data are expressed as the means ± SDs. A P value < 0.05 was considered statistically significant.

The work has been reported in line with the ARRIVE guidelines 2.0.

Results

Prediction and validation of circSPG21-miR-217-SIRT1 interactions

Bioinformatic analysis was utilized to identify differentially expressed circRNAs between normal and degenerative NP tissues via the microarray dataset GSE67566 from the Gene Expression Omnibus (GEO) database. Upregulated and downregulated circRNAs in degenerative tissues were visualized in a volcano plot (Fig. 1A), with significant changes represented by red and blue dots. The heatmap (Fig. 1B) highlights the expression levels of circRNAs, with a particular emphasis on circSPG21 (also known as hsa_circ_0003526 in CircBase), whose difference between normal and degenerative tissues is the most significant among the top ten downregulated circRNAs (Fig. S1B). Venn diagrams were used to illustrate the overlap of miRNAs associated with differentially expressed circRNAs across multiple databases. miR-217 was uniquely identified in both the CSCD and Interactome databases (Fig. 1C). The predicted target genes, including PM1D, SIRT1, KRAS, and DACH1, were common across RTarBase, miRecords, and TargetScan (Fig. 1D). For the four genes, the difference in the mRNA levels of SIRT1 between normal and degenerative tissues was the most pronounced (Fig. S1C). The network diagram (Fig. 1E) displays interactions between circSPG21, associated miRNAs, and their potential target genes. Sagittal T2-weighted MRI images of human NP tissue samples corresponding to Pfirrmann grades I through

(See figure on next page.)

Fig. 3 Upregulation of CircSPG21 alleviates TBHP-induced senescence in NPMSCs. **A** SA-β-Gal staining of NPMSCs from different groups (control, TBHP, TBHP + circSPG21, and TBHP + circSPG21-mut), showing senescent cells with blue-stained high SA-β-Gal expression (scale bar, 250 μm). **B** EdU assays of NPMSCs from different groups, where green fluorescence represents cells in a proliferating state and blue fluorescence indicates the cell nuclei (scale bar, 250 μm). **C** Quantitative analysis of EdU results, indicating changes in the proliferation rate among different groups. The data are expressed as the mean ± SD; *$P < 0.05$, **$P < 0.01$ indicates statistical significance, n = 6. **D**, **J** Western blot analysis and quantitative results showing the expression levels of the senescence- and mitophagy-associated proteins SIRT1, P21, P53, PINK1, and Parkin in NPMSCs across different groups, highlighting the effects of circSPG21 cotreatment. The data are expressed as the mean ± SD; *$P < 0.05$, **$P < 0.01$ indicates statistical significance, n = 6. Full-length blots/gels are presented in the Supplementary materials **E**, **F** Cell cycle analysis results of NPMSCs from different groups, illustrating the distribution of cells in various phases and the impact of circSPG21 on cell cycle arrest induced by TBHP. G0/G1 phase cells are represented by purple, S phase cells are represented by yellow, and G2/M phase cells are represented by green. **G** Fluorescence-based assessment of MMP in NPMSCs from different groups using JC-1 staining (scale bar, 50 μμm). Red fluorescence indicates mitochondrial aggregates (JC-1 aggregates), and green fluorescence indicates monomeric JC-1, reflecting MMP depolarization. **H** Quantitative analysis of JC-1 staining results, demonstrating changes in the MMP across different treatment groups. The data are expressed as the mean ± SD; *$P < 0.05$, **$P < 0.01$ indicates statistical significance, n = 6. **I** Quantitative analysis of SA-β-Gal staining, showing the percentage of senescent cells in each group. The data are expressed as the mean ± SD; *$P < 0.05$, **$P < 0.01$ indicates statistical significance, n = 6

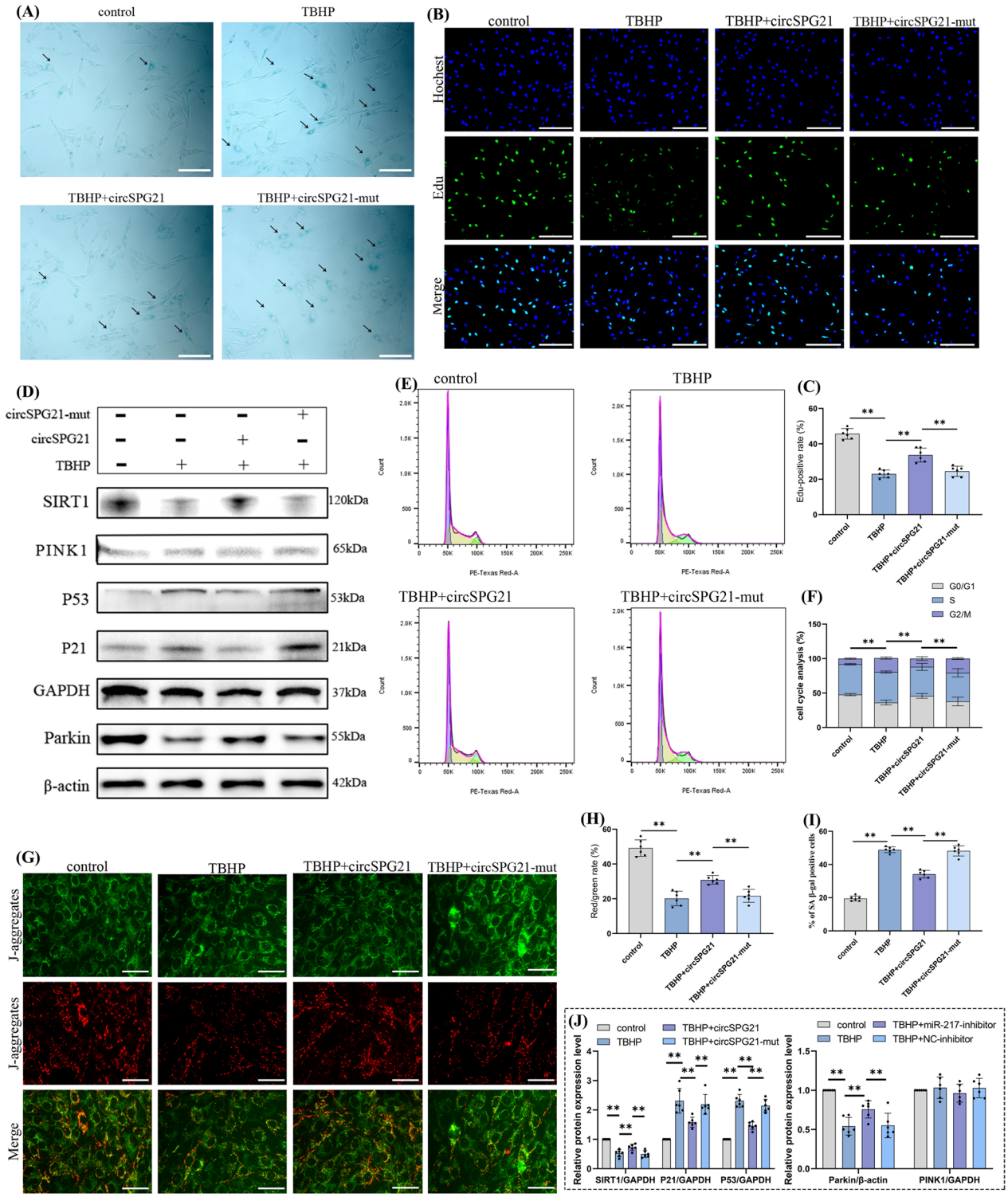

Fig. 3 (See legend on previous page.)

V (Fig. 1F) revealed varying disc morphologies and signal intensities, reflecting the variation in the severity of disc degeneration. Correlation analysis of these images and tissue samples revealed significant negative correlations between circSPG21 expression and the Pfirrmann grade (Fig. 1G), whereas the expression of miR-217

was positively correlated (Fig. 1H). The expression of SIRT1 was negatively correlated with the Pfirrmann grade (Fig. 1I), indicating that its reduction was associated with more severe degeneration. These findings were validated in a rat model of IVDD. MRI and HE-stained histological images (Fig. 1J) confirmed the successful establishment of the IVDD model, as evidenced by the observed degenerative changes. The results mirrored those in human samples, with significantly decreased levels of circSPG21 (Fig. 1K), increased levels of miR-217 (Fig. 1L), and decreased levels of SIRT1 (Fig. 1M) in the IVDD group compared with those in the control group. The expression of the top ten downregulated circRNAs between NPMSCs from normal and degenerative tissues was shown in Fig. S1D, with circSPG21 being the most significant.

Isolation and characterization of NPMSCs and validation of the TBHP-induced cell senescence model

Immunofluorescence analysis was performed to identify surface markers of isolated NPMSCs. The cells exhibited strong positive staining for the MSCs markers CD90, CD105, and CD73, as well as the NP cell marker Tie2, confirming their mesenchymal and NP origin (Fig. 2A). These cells were negative for CD34 and CD45, as indicated by the lack of significant fluorescence. The cells isolated from the rat coccygeal IVD displayed a long spindle shape. To assess the multipotency of the NPMSCs, we conducted differentiation assays to induce osteogenic, adipogenic, and chondrogenic differentiation (Fig. 2A). Osteogenic differentiation was confirmed by Alizarin Red staining for calcium deposits, adipogenic differentiation by Oil Red O staining for lipid droplets, and chondrogenic differentiation by Alcian blue staining for glycosaminoglycans. These results demonstrated that the NPMSCs could differentiate into multiple lineages, confirming their multipotent capacity in accordance with the standards proposed by the International Society for Cellular Therapy (ISCT). The CCK-8 assay results (Fig. 2B) revealed a dose- and time-dependent decrease in cell viability with increasing TBHP concentration. Significant reductions in cell viability were observed at 100 μM after 24 h, which was chosen as the optimal concentration for inducing cell injury in subsequent experiments. TBHP treatment significantly increased the percentage of SA-β-Gal-positive cells, indicating increased cellular senescence (Fig. 2C, E). Concurrently, the percentage of EdU-positive cells decreased markedly, reflecting reduced proliferation in the senescence model (Fig. 2D, F). These findings confirmed the successful establishment of the TBHP-induced cell senescence model. RT–qPCR analysis revealed that TBHP treatment significantly reduced circSPG21 expression (Fig. 2G), increased miR-217 levels (Fig. 2H), and decreased SIRT1 expression (Fig. 2I) in NPMSCs. NPMSCs were isolated from the tails of SD rats with healthy IVDs. FISH analysis, dual-luciferase assays and RIP demonstrated the binding abilities of circSPG21 with miR-217 and of miR-217 with SIRT1. For analysis of the functional implications of these interactions, the cells were divided into

(See figure on next page.)

Fig. 4 Downregulation of miR-217 mitigates TBHP-induced senescence in NPMSCs. **A** FISH analysis showing the localization of circSPG21 and miR-217 in NPMSCs. Blue fluorescence indicates the nucleus, green fluorescence marks circSPG21, and red fluorescence indicates miR-217, with both molecules predominantly located in the cytoplasm (scale bar, 250 μm). **B** RIP assay demonstrating the binding of circSPG21 and miR-217 to the Ago2 protein, suggesting a functional interaction between these molecules. The data are expressed as the mean ± SD; *$P < 0.05$, **$P < 0.01$ indicates statistical significance, n = 6. **C** The binding sites of miR-217 with circSPG21, predicted by TargetScan, are represented by the bold base sequences. Dual-luciferase assays of NPMSCs transfected with miR-217 and luciferase constructs of circSPG21, which contained either wild-type or mutated miR-217 binding sites, confirmed the direct targeting of circSPG21 by miR-217. The data are expressed as the mean ± SD; *$P < 0.05$, **$P < 0.01$ indicates statistical significance, n = 6. **D** EdU assay of NPMSCs from different groups (control, TBHP, TBHP + miR-217-inhibitor, and TBHP + NC-inhibitor), where green fluorescence represents proliferating cells and blue fluorescence marks the nuclei (scale bar, 250 μm). **E** Quantitative analysis of EdU results, demonstrating the effects of the miR-217 inhibitor on proliferation of the TBHP-treated NPMSCs. The data are expressed as the mean ± SD; *$P < 0.05$, **$P < 0.01$ indicates statistical significance, n = 6. **F** SA-β-Gal staining of NPMSCs from different groups (scale bar, 250 μm), showing blue-stained senescent cells with high SA-β-Gal expression. **G** Quantitative analysis of SA-β-Gal staining results, indicating reduced senescence in the miR-217-inhibitor treated cells. The data are expressed as the mean ± SD; *$P < 0.05$, **$P < 0.01$ indicates statistical significance, n = 6. **H**, **I** Cell cycle analysis of NPMSCs from different groups, illustrating changes in cell cycle distribution, particularly the reduction in G2/M phase arrest with miR-217 inhibitor treatment. G0/G1 phase cells are represented by purple, S phase cells are represented by yellow, and G2/M phase cells are represented by green. The quantitative data are expressed as the mean ± SD; *$P < 0.05$, **$P < 0.01$ indicates statistical significance, n = 6. **J** JC-1 staining results assessing MMP in different groups (scale bar, 50 μm), with red fluorescence representing mitochondrial aggregates (JC-1 aggregates) and green fluorescence indicating the monomeric form, reflecting MMP status. **K** Quantitative analysis of JC-1 staining, showing the impact of the miR-217 inhibitor on the mitochondrial membrane potential. The data are expressed as the mean ± SD; *$P < 0.05$, **$P < 0.01$ indicates statistical significance, n = 6. **L**, **M** Western blot analysis and quantitative results of the protein expression levels of SIRT1, P21, P53, PINK1, and Parkin in different groups, demonstrating the protective effect of the miR-217 inhibitor against TBHP-induced changes. The data are expressed as the mean ± SD; *$P < 0.05$, **$P < 0.01$ indicates statistical significance, n = 6. Full-length blots/gels are presented in the Supplementary materials

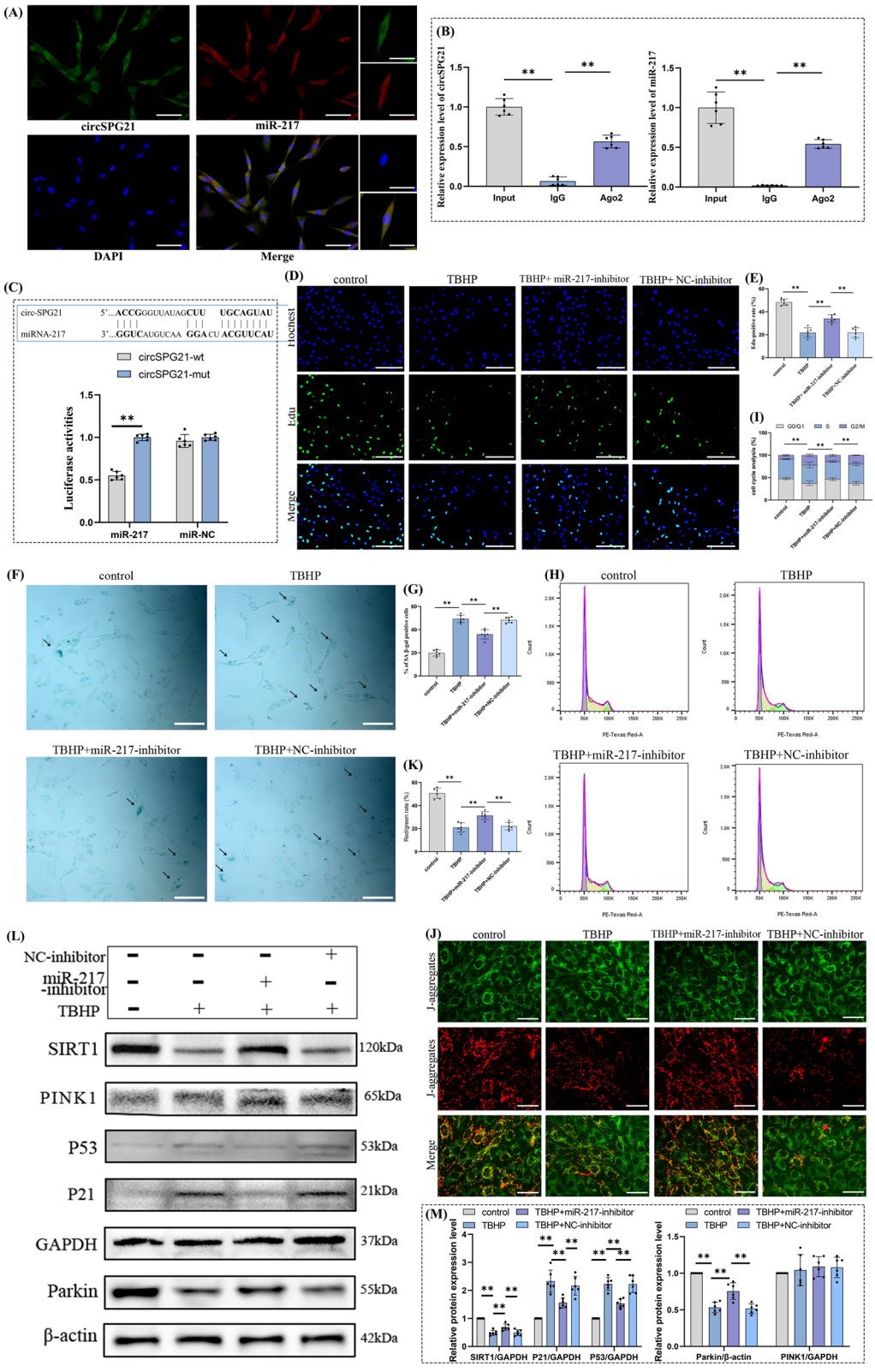

Fig. 4 (See legend on previous page.)

four experimental sections, with each section containing six dishes assigned via random number generation. Sect. "Background" describes the experimental groups (control, TBHP, TBHP + circSPG21, and TBHP + circSPG21-mut) and aims to demonstrate that the upregulation of circSPG21 alleviates TBHP-induced senescence in NPMSCs. Sect. "Methods" consists of the control, TBHP, TBHP + miR-217-inhibitor, and TBHP + NC-inhibitor groups, with a focus on the protective role of miR-217 downregulation against TBHP-induced senescence in NPMSCs. Sect. "Results" includes TBHP + circSPG21, TBHP + circSPG21 + SIRT1-shRNA, and TBHP + circSPG21 + NC-shRNA and examines the critical interaction between circSPG21 and SIRT1 in mitigating TBHP-induced senescence, with SIRT1 serving as a key mediator of the protective effects of circSPG21. Finally, Sect. "Discussion" comprises TBHP + miR-217-inhibitor, TBHP + miR-217-inhibitor + SIRT1-shRNA, and TBHP + miR-217-inhibitor + NC-shRNA, validating the role of SIRT1 as a key mediator in the protective effects of miR-217 inhibition against oxidative stress-induced cellular senescence and dysfunction. For analysis of these interactions, β-galactosidase staining, EdU staining, Western blotting, JC-1 assays, and cell cycle analysis were conducted on the above-mentioned samples (Fig. 2J).

The upregulation of circSPG21 alleviated TBHP-induced senescence in NPMSCs

SA-β-Gal staining was used to assess cellular senescence. CircSPG21 cotreatment reduced the percentage of SA-β-Gal-positive cells, demonstrating its protective role (Fig. 3A, I). EdU staining revealed that circSPG21 cotreatment partially restored the proliferation of NPMSCs (Fig. 3B, C). Cell cycle analysis revealed that circSPG21 significantly reduced the proportion of NPMSCs arrested in the G2/M phase under TBHP-induced oxidative stress (Fig. 3E, F). The MMP was assessed by JC-1 staining, which revealed that TBHP caused MMP depolarization, as indicated by reduced red and increased green fluorescence. CircSPG21 cotreatment partially preserved the MMP (Fig. 3G, H). Western blot analysis confirmed that circSPG21 cotreatment partially restored SIRT1 levels, reduced the expression of the senescence-associated proteins P21 and P53, and restored the levels of the mitophagy-related protein Parkin, highlighting the protective role of circSPG21 against cell senescence and its ability to modulate mitophagy in NPMSCs (Fig. 3D, J).

Downregulation of miR-217 mitigated TBHP-induced senescence in NPMSCs

The subcellular localization of circSPG21 and miR-217 was analyzed to infer their functional interaction. FISH analysis revealed that both circSPG21 and miR-217 are present in the cytoplasm, suggesting potential interactions within this cellular compartment (Fig. 4A). RIP assays further demonstrated the binding of circSPG21 and miR-217 to the Ago2 protein, indicating a regulatory relationship (Fig. 4B). The dual-luciferase assay confirmed that miR-217 directly targets circSPG21, highlighting its involvement in senescence regulation (Fig. 4C). EdU staining revealed that the miR-217 inhibitor restored NPMSCs proliferation in TBHP-treated cells, confirming that downregulation of miR-217 mitigated TBHP-induced cell senescence (Fig. 4D, E). Consistently, SA-β-Gal staining indicated that the miR-217 inhibitor reduced TBHP-induced cell senescence (Fig. 4F, G). Cell cycle analysis further revealed that the miR-217 inhibitor alleviated the G2/M phase arrest caused by TBHP (Fig. 4H, I). Additionally, JC-1 staining revealed that the miR-217 inhibitor preserved the MMP by preventing depolarization (Fig. 4J, K). Western blot analysis confirmed that compared with TBHP, the miR-217 inhibitor restored SIRT1 levels and decreased the expression levels of P21 and P53. The expression level of Parkin was partially restored, indicating that the miR-217 inhibitor preserves mitophagy, further supporting its protective role against cellular senescence (Fig. 4L, M).

(See figure on next page.)

Fig. 5 Effects of circSPG21 and SIRT1 on TBHP-induced senescence in NPMSCs. **A** EdU assay of NPMSCs in different treatment groups (TBHP + circSPG21, TBHP + circSPG21 + SIRT1-shRNA, and TBHP + circSPG21 + NC-shRNA). Green fluorescence indicates proliferating cells, while blue fluorescence marks the nuclei (scale bar, 250 μm). **B** SA-β-Gal staining of NPMSCs and quantitative analysis. Senescent cells exhibit blue-stained high expression of SA-β-Gal (scale bar, 250 μm). The quantitative data are expressed as the mean ± SD; *$P < 0.05$, **$P < 0.01$ indicates statistical significance, n = 6. **C** Fluorescence-based analysis of MMP in NPMSCs. Red fluorescence represents the mitochondrial aggregate JC-1, and green fluorescence indicates the monomeric JC-1. **D** Cell cycle analysis of NPMSCs in different groups. G0/G1 phase cells are represented by purple, S phase cells are represented by yellow, and G2/M phase cells are represented by green. The quantitative data are expressed as the mean ± SD; *$P < 0.05$, **$P < 0.01$ indicates statistical significance, n = 6. **E**, **H** Western blot analysis and quantification of the protein expression levels of SIRT1, P21, P53, PINK1, and Parkin in different groups. The quantitative data are expressed as the mean ± SD; *$P < 0.05$, **$P < 0.01$ indicates statistical significance, n = 6. Full-length blots/gels are presented in the Supplementary materials. **F** Quantitative analysis of EdU-positive cells across groups. The data are expressed as the mean ± SD; *$P < 0.05$, **$P < 0.01$ indicates statistical significance, n = 6. **G** Quantitative analysis of MMP results. The data are expressed as the mean ± SD; *$P < 0.05$, **$P < 0.01$ indicates statistical significance, n = 6

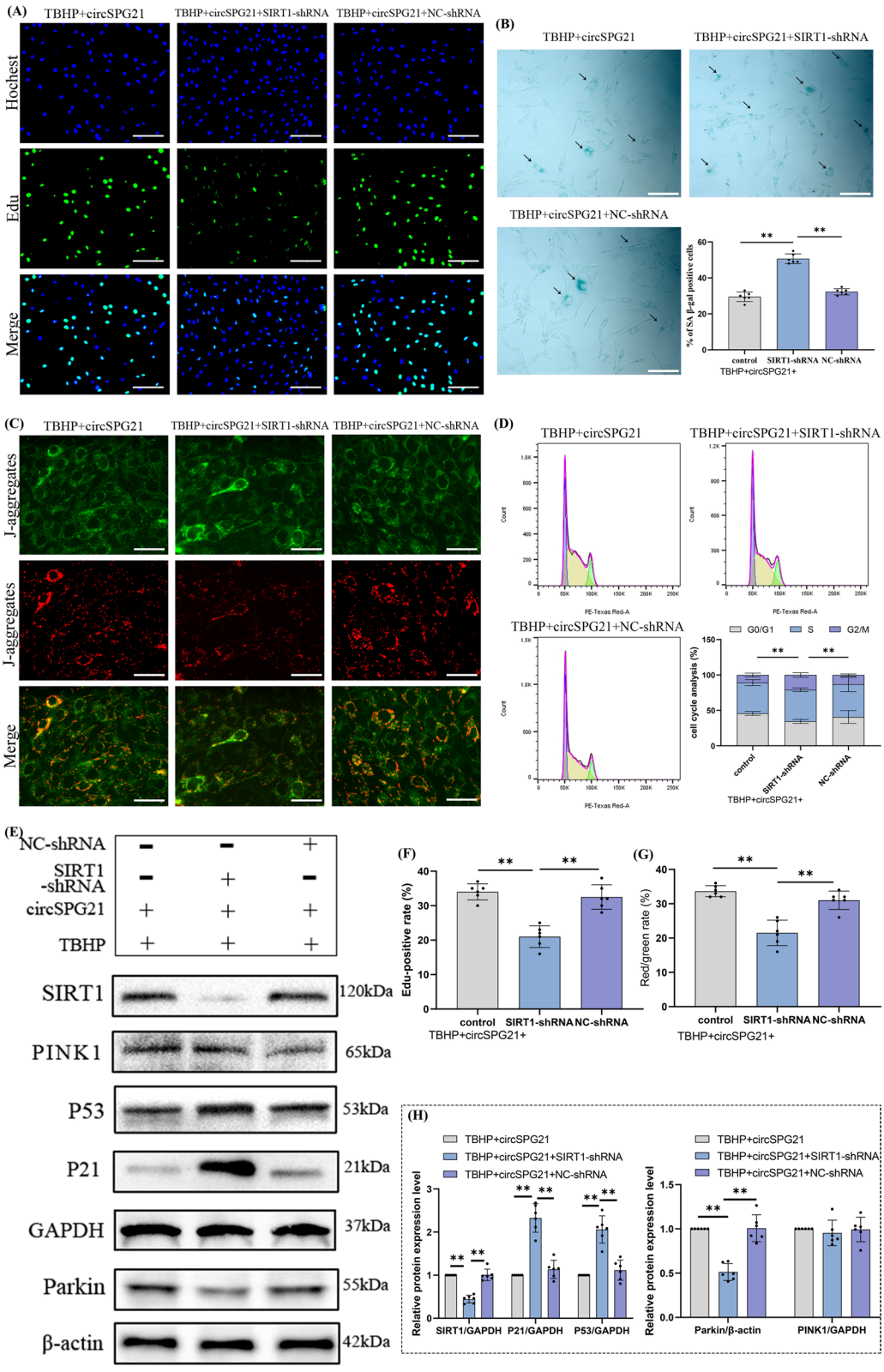

Fig. 5 (See legend on previous page.)

Identification of SIRT1 as a target of miR-217 and the miR-217/SIRT1 axis as a target of circSPG21

Further experiments explored the interactions among circSPG21, miR-217, and SIRT1 in mitigating TBHP-induced senescence in NPMSCs. EdU staining demonstrated that circSPG21 effectively promoted NPMSCs proliferation under oxidative stress, while this effect was significantly diminished by SIRT1-shRNA (Fig. 5A, F). Moreover, SIRT1-shRNA blocked the inhibitory effect of circSPG21 on NPMSCs senescence (Fig. 5B). The MMP results confirmed the crucial role of SIRT1 in maintaining mitochondrial polarization under oxidative stress, as the TBHP + circSPG21 + SIRT1-shRNA group exhibited significant mitochondrial depolarization compared with the TBHP + circSPG21 group (Fig. 5C, G). Cell cycle analysis further confirmed that knockdown of SIRT1 partially reversed the protective effects of circSPG21 on TBHP-induced G2/M phase arrest in NPMSCs (Fig. 5D). Western blot analysis supported these findings, showing that SIRT1 shRNA upregulated the senescence-associated proteins P21 and P53, thereby promoting TBHP-induced senescence. Additionally, the reduction in Parkin expression in the TBHP + circSPG21 + SIRT1-shRNA group highlighted the role of SIRT1 in modulating the protective effects of circSPG21 on mitophagy (Fig. 5E, H).

The dual-luciferase assay confirmed that miR-217 binds to the 3' UTR of SIRT1, establishing SIRT1 as a direct target of miR-217 (Fig. 6A). This interaction was further supported by the results of the EdU assay, which demonstrated that SIRT1-shRNA significantly decreased the EdU-positive rate, indicated that silencing SIRT1 suppressed the protective effects of the miR-217 inhibitor on cell proliferation (Fig. 6B, G). Western blot analysis revealed that SIRT1-shRNA antagonized the protective effects of the miR-217 inhibitor, as indicated by increased levels of the senescence-associated proteins P21 and P53, along with a reduction in the mitophagy-related protein Parkin (Fig. 6C, H). Similarly, the MMP results revealed that in the TBHP + miR-217-inhibitor + SIRT1-shRNA group, there was a marked reduction in the red/green fluorescence ratio, suggesting that SIRT1 is essential for maintaining the MMP under conditions of miR-217 knockdown (Fig. 6D, I). SA-β-Gal staining further supported these findings, revealing a significantly greater percentage of SA-β-Gal-positive cells in the TBHP + miR-217-inhibitor + SIRT1-shRNA group than in the TBHP + miR-217-inhibitor group (Fig. 6E). Additionally, cell cycle analysis revealed that SIRT1-shRNA reversed the alleviation of G2/M phase arrest observed under miR-217 knockdown conditions, further highlighting the role of SIRT1 in regulating the cell cycle (Fig. 6F).

CircSPG21 alleviated IVDD in a rat model

A rat model of IVDD was established via a fine needle puncture technique. Two weeks after the puncture, transfection solutions containing circSPG21 or circSPG21-mut were injected into the degenerated disc segments. Four weeks post-injection, the rats were euthanized for radiological and histological analyses (Fig. 7A). Compared with the Con group, the IVDD group presented a significant decrease in DHI, whereas the IVDD + circSPG21 group presented a greater DHI than the IVDD group did (Fig. 7B–D). MRI scans, which are utilized for Pfirrmann grading, revealed higher grades in the IVDD group, while the IVDD + circSPG21 group exhibited a significant reduction in the Pfirrmann grade at 6 weeks compared with the IVDD group (Fig. 7E, F). HE staining (Fig. 7G) revealed that NP tissues occupied most of the disc area, with well-dispersed NP cells and a well-organized AF in the control group. In contrast, the IVDD group exhibited nearly complete loss of NP tissues and severe disruption of the NP-AF border, which was partially mitigated by circSPG21 treatment. Safranin-O staining revealed a reduction in the proteoglycan matrix area in the IVDD group compared with the control group, but

(See figure on next page.)

Fig. 6 Identification of SIRT1 as a target of miR-217 and the functional impact on NPMSCs. **A** The binding sites of miR-217 with the mRNA of SIRT1, predicted by TargetScan, are represented by the bold base sequences. Dual-luciferase reporter assay showing the interaction of miR-217 with the wild-type and mutated binding sites of the SIRT1 3' UTR in transfected NPMSCs. The data are expressed as the mean ± SD; *$P < 0.05$, **$P < 0.01$ indicates statistical significance, n = 6. **B** EdU assay of NPMSCs under various treatment conditions (TBHP + miR-217-inhibitor, TBHP + miR-217-inhibitor + SIRT1-shRNA, and TBHP + miR-217-inhibitor + NC-shRNA). Green fluorescence indicates cells in a proliferating state, and blue fluorescence represents cell nuclei (scale bar, 250 μm). **C**, **H** Western blot analysis and quantification of the protein expression levels of SIRT1, P21, P53, PINK1, and Parkin across different groups. Full-length blots/gels are presented in the Supplementary materials. **D** Analysis of MMP in different groups, detected by fluorescence (scale bar, 50 μm). Red fluorescence corresponds to aggregated JC-1, and green fluorescence indicates monomeric JC-1. **E** SA-β-Gal staining of NPMSCs (scale bar, 250 μm) and quantitative analysis, highlighting the high expression of SA-β-Gal in senescent cells (blue staining). The quantitative data are expressed as the mean ± SD; *$P < 0.05$, **$P < 0.01$ indicates statistical significance, n = 6. **F** Flow cytometry analysis of cell cycle distribution in NPMSCs under different conditions, including quantitative results. The quantitative data are expressed as the mean ± SD; *$P < 0.05$, **$P < 0.01$ indicates statistical significance, n = 6. **G** Quantitative analysis of EdU-positive cells. The data are expressed as the mean ± SD; *$P < 0.05$, **$P < 0.01$ indicates statistical significance, n = 6. **I** Quantitative analysis of MMP results. The data are expressed as the mean ± SD; *$P < 0.05$, **$P < 0.01$ indicates statistical significance, n = 6

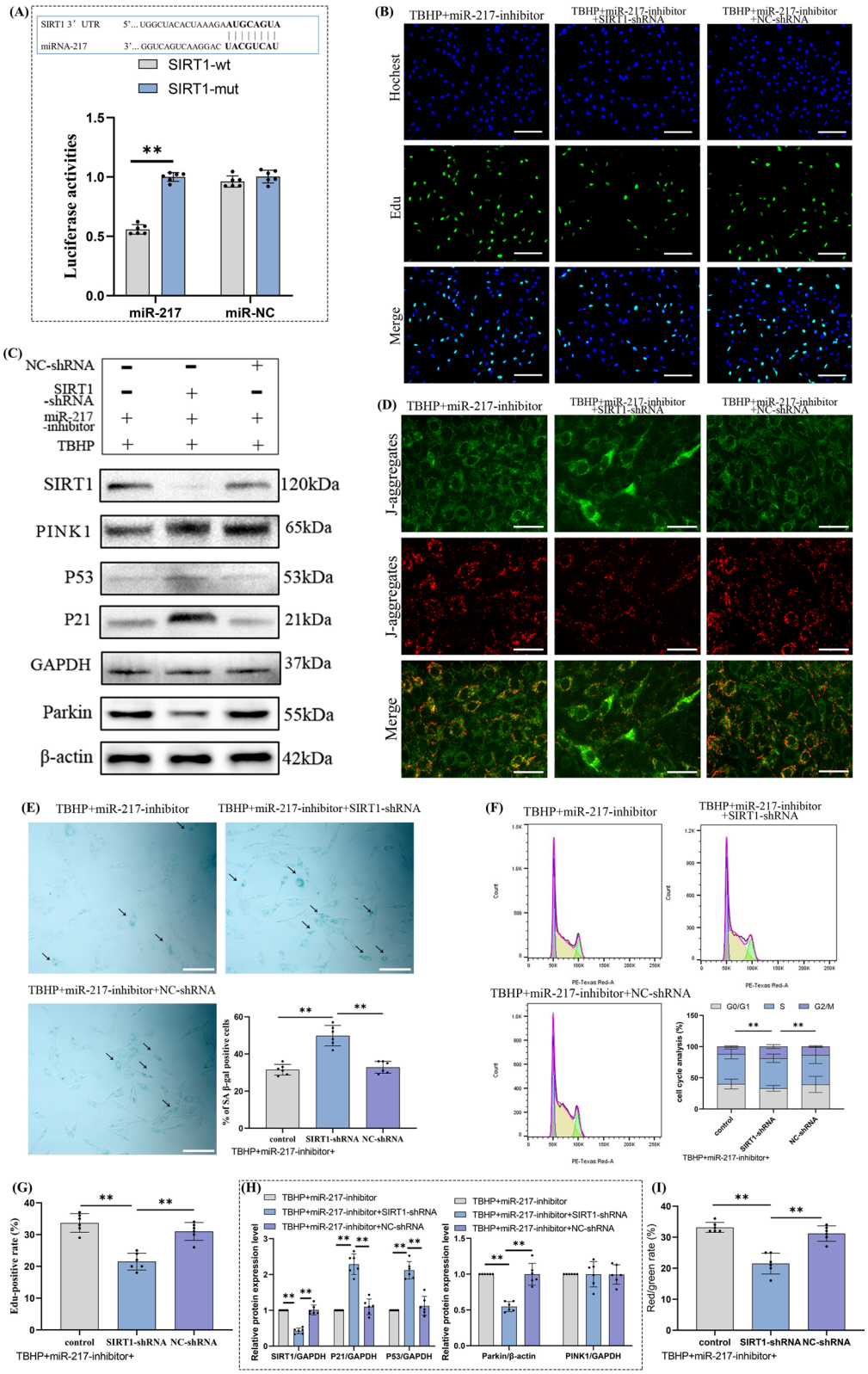

Fig. 6 (See legend on previous page.)

this reduction was alleviated in the IVDD + circSPG21 group (Fig. 7H). The histological scores (Fig. 7I) were significantly greater in the IVDD group than in the Con group, whereas the IVDD + circSPG21 group presented lower scores. RT–qPCR analysis revealed that circSPG21 levels were lower in the IVDD group than in the Con group but were significantly restored in the IVDD + circSPG21 group (Fig. 7J). Similarly, miR-217 levels were elevated in the IVDD group but were notably reduced in the IVDD + circSPG21 group (Fig. 7K). The levels of SIRT1, which were diminished in the IVDD group, were strongly restored in the IVDD + circSPG21 group (Fig. 7L).

Discussion

The development and progression of IVDD are closely linked to the senescence of NPMSCs, a type of endogenous cell in NP tissue whose importance has not yet been adequately recognized [57]. The senescence of NPMSCs is driven by multiple signaling pathways and molecular mechanisms, including oxidative stress and mitochondrial dysfunction [14, 58]. The interplay of these mechanisms makes it challenging to fully arrest the senescence process through the regulation of a single pathway. The adverse microenvironment of degenerated discs further accelerates NPMSCs senescence, and genetic regulation alone cannot counteract the effects of this microenvironment [59]. Moreover, genetic regulation techniques such as overexpression or gene knockout can delay cellular senescence under laboratory conditions but are unstable when applied in vivo [60, 61]. Thus, identifying novel approaches to mitigate NPMSCs senescence is crucial.

Moreover, multiple lines of evidence suggest that circRNAs can act as molecular sponges in conjunction with miRNAs to modulate the expression of target genes and are thus involved in the initiation and progression of IVDD [62, 63]. Our findings demonstrated that circSPG21 significantly mitigates NPMSCs senescence and promotes mitophagy under oxidative stress, specifically through the miR-217/SIRT1 axis (Fig. 8), thereby providing new insights into the potential therapeutic application of circSPG21 in IVDD.

The role of oxidative stress in the pathogenesis of IVDD is well documented, with research indicating that targeting oxidative stress could offer potential therapeutic avenues for IVDD [64, 65]. Oxidative stress can lead to oxidative damage in the extracellular matrix, DNA, and mitochondria of IVD cells [66]. The rupture of AF activates oxidative stress, the immune response and apoptosis in NPCs [67]. Oxidative stress within the IVD microenvironment promotes NPMSCs senescence, diminishing the pluripotency and self-renewal abilities of senescent NPMSCs, which in turn reduces the regenerative potential and endogenous repair capability of NPMSCs [68, 69]. Therefore, TBHP was used to induce oxidative stress in NPMSCs, resulting in cellular senescence, and a punctured rat IVDD model was selected to evaluate the function of circSPG21 in vivo.

Cellular senescence is associated with many degenerative diseases and is typically induced by the P21/P53 pathway accompanied by an increase of SA-β-gal, arrest of G2/M and a decrease in the cell proliferation rate [70–72], accompanied by a decrease in the mitochondrial membrane potential and impaired mitophagy [73, 74]. Hence, the indices mentioned above were measured in this study as key markers of senescence. Oxidative stress induces senescence in NPCs, and circKIF18A upregulation can mitigate this effect via MCM7 [75]. In our earlier studies, several drugs (such as quercetin and urolithin A) were shown to relieve oxidative stress-induced senescence and alleviate IVDD in an in vitro rat model [19, 21]. However, the underlying mechanisms are still unclear. In the present study, we found increased expression of senescence-related proteins (p21 and p53), increased SA-β-Gal-positive senescent cells, decreased mitophagy, decreased MMP and decreased proliferation after TBHP treatment in NPMSCs, which could be mitigated by

(See figure on next page.)

Fig. 7 CircSPG21 alleviated IVDD in vivo. **A** Schematic of the in vivo experiment process, detailing the establishment of the IVDD model and the subsequent injection of circSPG21 or circSPG21-mut into the degenerated disc segments. **B** Measurements of the IVD height index (DHI). The anterior, middle, and posterior heights of the disc and adjacent vertebrae were measured, and then, the sum of the disc heights was doubled and divided by the sum of the vertebral heights to obtain the DHI. **C** Representative X-ray images of rat lumbar spines at 0 week and 6 weeks post-puncture in different groups. **D** Quantitative analysis of DHI, illustrating the disc height changes among the control, IVDD, IVDD + circSPG21 and IVDD + circSPG21-mut groups. The quantitative data are expressed as the mean ± SD; *$P < 0.05$, **$P < 0.01$ indicates statistical significance, n = 6. **E** MRI scans of the discs at 0 weeks and 6 weeks post-puncture, used to assess disc degeneration grade. **F** Quantitative analysis of Pfirrmann grades, demonstrating the effect of circSPG21 on reducing degenerative severity compared to that of the IVDD group. The quantitative data are expressed as the mean ± SD; *$P < 0.05$, **$P < 0.01$ indicates statistical significance, n = 6. **G–I** Representative images of haematoxylin and eosin (H&E) and Safranin O (S–O) stained sections (scale bar, 1 mm), along with the quantitative histological scores. The staining reveals the structural integrity of NP and annulus fibrosus (AF) and matrix composition in different groups. The quantitative data are expressed as the mean ± SD; *$P < 0.05$, **$P < 0.01$ indicates statistical significance, n = 6. J-L: RT–qPCR analysis showing the expression levels of circSPG21, miR-217, and SIRT1 in rat NP tissues, indicating the regulatory effects of circSPG21 on these molecular markers in the context of disc degeneration. The data are expressed as the mean ± SD; *$P < 0.05$, **$P < 0.01$ indicates statistical significance, n = 6

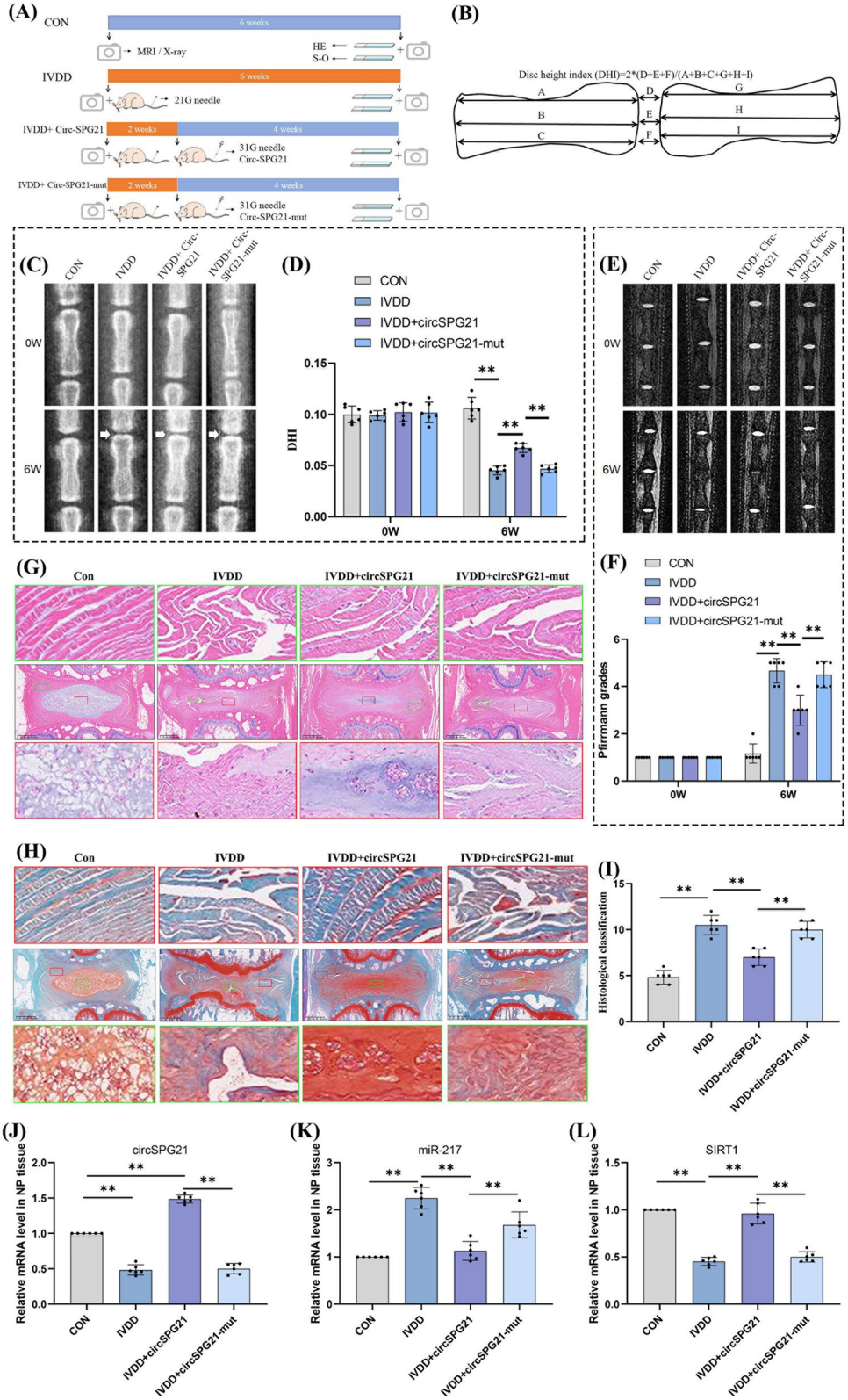

Fig. 7 (See legend on previous page.)

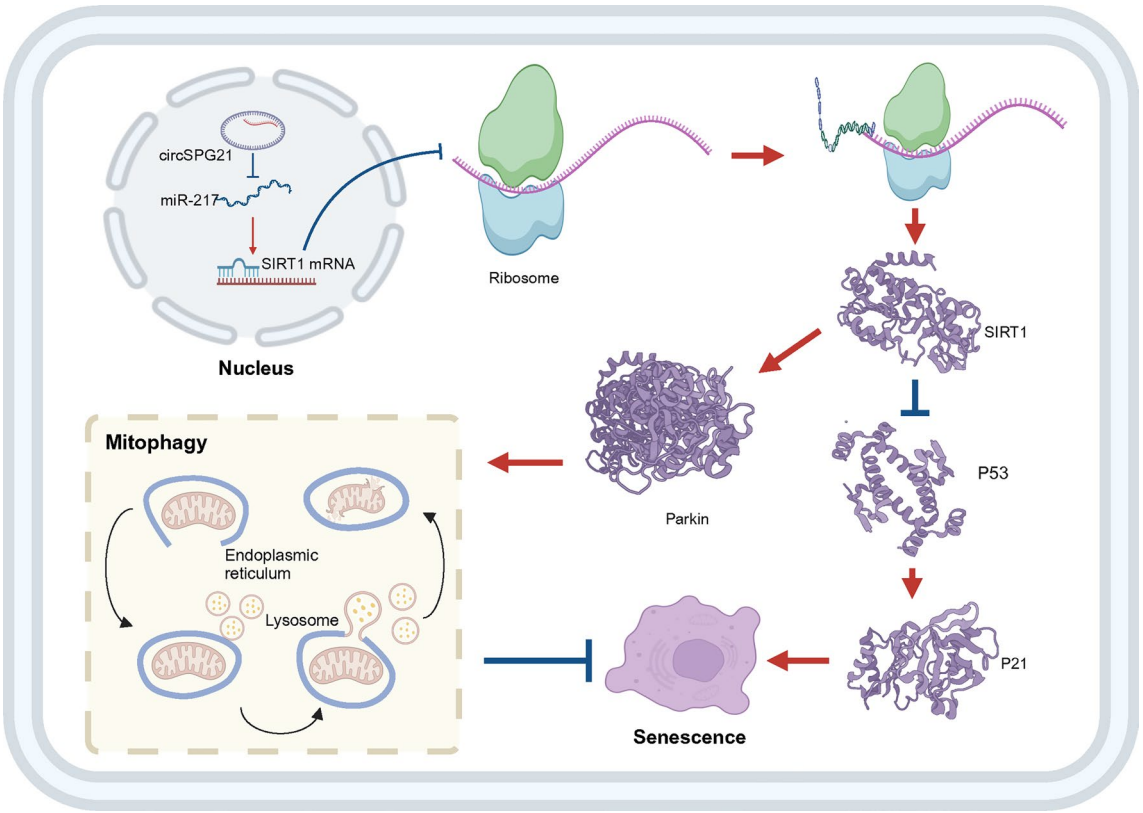

Fig. 8 Schematic of the working hypothesis; miR-217 competitively inhibits SIRT1 mRNA, thereby suppressing SIRT1 protein expression, which further promotes NPMSCs senescence via P21/P53 and inhibits mitophagy through Parkin. circSPG21 acts as a molecular sponge for miR-217, inhibiting the suppressive effect of miR-217 on SIRT1, and indirectly alleviating NPMSCs senescence through P53/P21 and Parkin-mediated mitophagy

circSPG21. These findings demonstrated that oxidative stress caused senescence accompanied by mitochondrial dysfunction in NPMSCs and that this effect can be mitigated by circSPG21.

Mitophagy, a selective autophagic process that specifically removes dysfunctional mitochondria to ensure mitochondrial quality control [76], is essential for cellular health and closely related to degenerative joint diseases such as osteoarthritis and IVDD [66, 76]. Studies have shown mitochondrial dysfunction and increased SA-β-Gal in human degenerated IVDs, while the NLRX1-SLC39A7 complex can mitigate NPC degeneration by increasing mitophagy via the regulation of mitochondrial Zn^{2+} transport [77]. The PRKN-dependent pathway, which is mediated by PINK1 and Parkin, is one of the main mechanisms regulating mitophagy [78]. Under conditions of mitochondrial damage, PINK1 accumulates on the mitochondrial outer membrane and recruits Parkin, an E3 ubiquitin ligase, which then tags damaged mitochondria for degradation [78]. PINK1/Parkin is elevated in degenerated NP tissues and NPCs treated with H_2O_2, suggesting mitophagic activation in IVDD and under oxidative stress [12, 79]. EGR1 knockdown inhibits NPCs senescence and mitochondrial damage through the activation of PINK1-Parkin-dependent mitophagy, thereby delaying IVDD [80]. Therefore, mitophagy can maintain mitochondrial function and alleviate damage and senescence in NPCs, with the PINK/Parkin pathway playing an important role. However, the role of mitophagy in NPMSCs remains poorly understood. The expression levels of Parkin and PINK1 were used as key markers to evaluate mitophagy. This study revealed that the expression of Parkin was decreased after TBHP treatment, which could be mitigated by circSPG21 or decreased miR-217. Therefore, circSPG21 alleviated NPMSCs senescence induced by oxidative stress by promoting mitophagy, thereby preserving mitochondrial function and reducing cellular damage.

Multiple circRNAs have been confirmed to be involved in IVDD, with some showing protective effects and others exacerbating IVDD. For example, circVMA21 was found to function in NPCs to prevent apoptosis by targeting miR-200c and XIAP in our prior studies [26]. Additionally, circEYA3 promotes ECM degradation and apoptosis

in NPCs via the miR-196a-5p/EBF1 axis and the NF-κB pathway [81]. In this study, circSPG21 was found to be associated with the severity of IVDD and exhibited significant differences in expression in both the IVDD rat model and the NPMSCs senescence model. Bioinformatic analysis revealed that circSPG21 contains miR-217 target sites and that miR-217 contains mRNAs with SIRT1 target sites, which was verified by dual-luciferase analysis, FISH and RIP. In addition, the effects of circSPG21 can be inhibited by SIRT1-shRNA. Therefore, we propose that the effects of circSPG21 are mediated by the miR-217/SIRT1 axis. The present study revealed that the overexpression of circSPG21 significantly decreased the degree of senescence and increased mitophagy of NPMSCs under TBHP treatment, suggesting that circSPG21 is beneficial for the survival of NPMSCs under oxidative stress. Accordingly, circSPG21 overexpression alleviated IVDD in a rat model in vivo. In the previous study, CircSPG21 (hsa_circ_0035875 in circBase) can protect against extracellular matrix degradation in human NPCs by targeting the miR-1197/ATP1B3 axis [62]. Our study provides the first detailed investigation into the role of CircSPG21 (hsa_circ_0003526 in circBase) in IVDD, contrasting with the earlier findings related to hsa_circ_0035875. The two isoforms have molecular differences and appear to function via different pathways in different cells—while hsa_circ_0035875 modulates matrix degradation in NPCs, hsa_circ_0003526 regulates mitochondrial function and senescence in NPMSCs. In addition, hsa_circ_0035875 contains a miR-1197 binding site and functioned as a ceRNA effect through ATP1B3, while hsa_circ_0003526 contains a miR-217 binding site and exerted its effect through SIRT1. This distinction is particularly important in understanding the multifaceted roles of circRNAs and that circSPG21 is a promising therapeutic target for NPMSCs senescence and IVDD.

Various miRNAs have been confirmed to play roles in IVDD. The overexpression of miR-558 can suppress NPCs proliferation and ECM synthesis, which can be suppressed by hsa_circ_0083756 functioning as a ceRNA [82]. Induced pluripotent stem cell-derived MSCs can deliver exogenous miR-105-5p via small extracellular vesicles to rejuvenate senescent NPCs [83]. miR-217 was shown to be present in exosomes derived from senescent epithelial cells and activates pulmonary fibroblasts via SIRT1 in paraquat-induced pulmonary fibrosis [84]. Downregulation of miR-217 can also alleviate myocardial ischaemia–reperfusion injury by remodeling mitochondrial function through SIRT1, and the ability of miR-217 to bind to SIRT1 has also been confirmed [85]. Although miR-217 has been extensively researched in numerous human senescence-related diseases, this is the first study of the role of miR-217 in the senescence of NPMSCs [85, 86]. The present study demonstrated the ability of miR-217 to bind to SIRT1 and revealed that the ability of miR-217 to decrease NPMSCs senescence and promote mitophagy could be inhibited by SIRT1-shRNA, suggesting that these effects were related to the regulatory effect of circSPG21 on the miR-217/SIRT1 axis.

As a deacetylase, SIRT1 plays an important role in alleviating cellular senescence and degenerative diseases [76, 87]. The overexpression of SIRT1 can ameliorate IL-1β-induced mitochondrial dysfunction and ROS accumulation and inhibit NLRP3 inflammasome activation by promoting PINK1/Parkin-mediated mitophagy [88]. Additionally, SIRT1 can regulate cellular senescence through pathways such as haem oxygenase-1 (HO-1), nuclear factor erythroid 2–related factor 2 (Nrf2), and phosphoinositide 3-kinase (PI3K), with Parkin-mediated mitophagy being one of the important mechanisms [89–91]. In our previous studies, SIRT1 was shown to act with miR-34a-5p or peroxisome proliferator-activated receptor γ coactivator 1-alpha (PGC1-α) to reduce oxidative stress-induced senescence in NPMSCs [19, 21]. These findings indicate that SIRT1 has a protective role in preserving the cellular function and viability of NPMSCs in response to oxidative stress. In this study, SIRT1 was confirmed to be regulated by circSPG21 through miR-217. Additionally, SIRT1-shRNA can reduce Parkin-mediated mitophagy and promote cellular senescence caused by circSPG21 and miR-217, indicating that the protective effects on NPMSCs mitophagy and senescence are related to the regulatory effects of circSPG21 on the miR-217/SIRT1 axis.

This study also has certain limitations. Although circSPG21 was confirmed to alleviate IVDD progression in an IVDD model, it is still unclear whether it regulates IVDD by affecting NPMSCs senescence. In addition to its ceRNA function, circSPG21 may have other potential mechanisms for regulating IVDD, such as interacting with RNA-binding proteins [92] or influencing other signaling pathways. Moreover, circSPG21 expression tends to decrease in both the NPMSCs oxidative stress-induced senescence model and in human degenerative NP tissues, but the upstream regulatory mechanisms that control its expression are not fully understood. Future studies should focus on elucidating these regulatory networks and exploring the broader impact of circSPG21 on NPMSCs biology and IVDD. This research could reveal new therapeutic targets and pave the way for the development of circSPG21-based treatments.

Conclusion

This study highlights the critical role of circSPG21 in mitigating NPMSCs senescence and promoting mitophagy under oxidative stress, primarily through the miR-217/

SIRT1 axis. Due to its ability to increase mitophagy and reduce cellular senescence, circSPG21 is a promising therapeutic target for NPMSCs senescence, providing a novel approach to preserving IVD health. Further research on the regulatory mechanisms of circSPG21 and its broader impact on cellular senescence and stress responses could lead to innovative therapies for IVDD and related degenerative conditions.

Supplementary Information

The online version contains supplementary material available at https://doi.org/10.1186/s13287-025-04180-1.

Additional file 1.

Additional file 2.

Acknowledgements
The authors thank the Northern Jiangsu People's Hospital and Graduate School of Dalian Medical University for the consultation and instrument availability that supported this work.

Author contributions
All the authors contributed to the study conception and design. Data curation, Yongbo Zhang, Sheng Yang, Liuyang Chen and Xuan You; formal analysis, Yongbo Zhang and Sheng Yang; funding acquisition, Liang Zhang; methodology, Sheng Yang and Zhengguang Li; project administration, Liang Zhang; software, Xuan You; validation, Liuyang Chen; visualization, Liang Zhang and Rui Dai; writing-original draft, Yongbo Zhang, Sheng Yang, Liuyang Chen, Xuan You and Hua Sun; writing-review & editing, Yongbo Zhang, Liang Zhang, Rui Dai and Sheng Yang. All the authors drafted and reviewed the manuscript.

Funding
This work was supported by the National Natural Science Foundation of China (Grant No. 82172462 to LZ), the Traditional Chinese Medicine Science and Technology Development Plan Project of Jiangsu Province (Grant No. YB2020085 to LZ), the Sixth "333 Project" Outstanding Young Talent Scientific Research Project of Jiangsu Province (Grant No. 11 to LZ), the Cross Cooperation Special Project of Northern Jiangsu People's Hospital (Grant No. SBJC21014 to LZ) and Key Projects of Social Development of Yangzhou City (Grant No. YZ2021083/ YZ2022091 to LZ).

Data availability
The data that support the findings of this study are openly available in [repository name e.g., "GEO"] at https://www.ncbi.nlm.nih.gov/geo/, reference number [GSE67566]. Full-length blots/gels are presented in Supplementary materials.

Declarations

Ethics approval and consent to participate
The study titled "*The mechanism of circ-SPG21 acting as a ceRNA in the regulation of miRNA-217 in the degeneration of intervertebral disc through endogenous NPMSC senescence*" was approved by the Animal Ethics Committee of Yangzhou University (Approval No. 2021ky050) on February 22, 2021. Additionally, the study protocol was approved by the Ethics Committee of the Northern Jiangsu People's Hospital (Approval No. 202103427) on March 2, 2021. Informed consent was obtained from all individual participants included in the study.

Consent to publish
Our manuscript does not contain any individual person's data in any form (including any individual details, images or videos).

Competing interests
The authors have no relevant financial or nonfinancial interests to disclose.

AI use declaration
The authors declare that they have not use AI-generated work in this manuscript.

Author details
[1]Dalian Medical University, Dalian 116000, China. [2]Department of Orthopedics, The Yangzhou School of Clinical Medicine of Dalian Medical University, Yangzhou 225001, China. [3]Department of Orthopedics, Northern Jiangsu People's Hospital, Yangzhou 225001, China. [4]Department of Orthopedics, Northern Jiangsu People's Hospital Affiliated to Yangzhou University, No.98 Nantong West Road, Yangzhou 225001, Jiangsu Province, China. [5]Department of Orthopedics, The Yangzhou Clinical Medical College of Xuzhou Medical University, Yangzhou 225001, China.

Received: 2 October 2024 Accepted: 23 January 2025
Published online: 07 February 2025

References

1. Disease GBD, Injury I, Prevalence C. Global, regional, and national incidence, prevalence, and years lived with disability for 354 diseases and injuries for 195 countries and territories, 1990–2017: a systematic analysis for the global burden of disease study 2017. Lancet. 2018;392(10159):1789–858.
2. Bydon M, De la Garza-Ramos R, Macki M, Baker A, Gokaslan AK, Bydon A. Lumbar fusion versus nonoperative management for treatment of discogenic low back pain: a systematic review and meta-analysis of randomized controlled trials. J Spinal Disord Tech. 2014;27(5):297–304.
3. Richardson SM, Kalamegam G, Pushparaj PN, Matta C, Memic A, Khademhosseini A, Mobasheri R, Poletti FL, Hoyland JA, Mobasheri A. Mesenchymal stem cells in regenerative medicine: focus on articular cartilage and intervertebral disc regeneration. Methods. 2016;99:69–80.
4. Ukeba D, Sudo H, Tsujimoto T, Ura K, Yamada K, Iwasaki N. Bone marrow mesenchymal stem cells combined with ultra-purified alginate gel as a regenerative therapeutic strategy after discectomy for degenerated intervertebral discs. EBioMedicine. 2020;53:102698.
5. Borem R, Madeline A, Bowman M, Gill S, Tokish J, Mercuri J. Differential effector response of amnion- and adipose-derived mesenchymal stem cells to inflammation; implications for intradiscal therapy. J Orthop Res. 2019;37(11):2445–56.
6. Wu H, Zeng X, Yu J, Shang Y, Tu M, Cheang LH, Zhang J. Comparison of nucleus pulposus stem/progenitor cells isolated from degenerated intervertebral discs with umbilical cord derived mesenchymal stem cells. Exp Cell Res. 2017;361(2):324–32.
7. Liu Y, Li Y, Huang ZN, Wang ZY, Nan LP, Wang F, Zhou SF, Wang JC, Feng XM, Zhang L. The effect of intervertebral disc degenerative change on biological characteristics of nucleus pulposus mesenchymal stem cell: an in vitro study in rats. Connect Tissue Res. 2019;60(4):376–88.
8. Risbud MV, Guttapalli A, Tsai TT, Lee JY, Danielson KG, Vaccaro AR, Albert TJ, Gazit Z, Gazit D, Shapiro IM. Evidence for skeletal progenitor cells in the degenerate human intervertebral disc. Spine (Phila Pa 1976). 2007;32(23):2537–44.
9. Lyu FJ, Cheung KM, Zheng Z, Wang H, Sakai D, Leung VY. IVD progenitor cells: a new horizon for understanding disc homeostasis and repair. Nat Rev Rheumatol. 2019;15(2):102–12.
10. Yi W, Lan H, Wen Y, Wang Y, He D, Bai Z, Zhang Y, Jiang W, Liu B, Shen J, et al. HO-1 overexpression alleviates senescence by inducing autophagy

via the mitochondrial route in human nucleus pulposus cells. J Cell Physiol. 2020;235(11):8402–15.
11. Vergroesen PP, Kingma I, Emanuel KS, Hoogendoorn RJ, Welting TJ, van Royen BJ, van Dieen JH, Smit TH. Mechanics and biology in intervertebral disc degeneration: a vicious circle. Osteoarthr Cartil. 2015;23(7):1057–70.
12. Huang D, Peng Y, Li Z, Chen S, Deng X, Shao Z, Ma K. Compression-induced senescence of nucleus pulposus cells by promoting mitophagy activation via the PINK1/PARKIN pathway. J Cell Mol Med. 2020;24(10):5850–64.
13. He R, Wang Z, Cui M, Liu S, Wu W, Chen M, Wu Y, Qu Y, Lin H, Chen S, et al. HIF1A alleviates compression-induced apoptosis of nucleus pulposus derived stem cells via upregulating autophagy. Autophagy. 2021;17(11):3338–60.
14. Sakai D, Nakamura Y, Nakai T, Mishima T, Kato S, Grad S, Alini M, Risbud MV, Chan D, Cheah KS, et al. Exhaustion of nucleus pulposus progenitor cells with ageing and degeneration of the intervertebral disc. Nat Commun. 2012;3:1264.
15. Wu H, Shang Y, Yu J, Zeng X, Lin J, Tu M, Cheang LH, Zhang J. Regenerative potential of human nucleus pulposus resident stem/progenitor cells declines with ageing and intervertebral disc degeneration. Int J Mol Med. 2018;42(4):2193–202.
16. Dimozi A, Mavrogonatou E, Sklirou A, Kletsas D. Oxidative stress inhibits the proliferation, induces premature senescence and promotes a catabolic phenotype in human nucleus pulposus intervertebral disc cells. Eur Cell Mater. 2015;30:89–102.
17. Jiang LB, Cao L, Ma YQ, Chen Q, Liang Y, Yuan FL, Li XL, Dong J, Chen N. TIGAR mediates the inhibitory role of hypoxia on ROS production and apoptosis in rat nucleus pulposus cells. Osteoarthr Cartil. 2018;26(1):138–48.
18. Wang J, Huang Y, Luan T, Shi P, Guo L, Zhang Q, Shi G, Hao Z, Chen T, Zhang L, et al. Hydrogel and microgel collaboration for spatiotemporal delivery of biofactors to awaken nucleus pulposus-derived stem cells for endogenous repair of disc. Small. 2024;20:e2404732.
19. Shi PZ, Wang JW, Wang PC, Han B, Lu XH, Ren YX, Feng XM, Cheng XF, Zhang L. Urolithin a alleviates oxidative stress-induced senescence in nucleus pulposus-derived mesenchymal stem cells through SIRT1/PGC-1alpha pathway. World J Stem Cells. 2021;13(12):1928–46.
20. Li XC, Wang MS, Liu W, Zhong CF, Deng GB, Luo SJ, Huang CM. Co-culturing nucleus pulposus mesenchymal stem cells with notochordal cell-rich nucleus pulposus explants attenuates tumor necrosis factor-alpha-induced senescence. Stem Cell Res Ther. 2018;9(1):171.
21. Zhao WJ, Liu X, Hu M, Zhang Y, Shi PZ, Wang JW, Lu XH, Cheng XF, Tao YP, Feng XM, et al. Quercetin ameliorates oxidative stress-induced senescence in rat nucleus pulposus-derived mesenchymal stem cells via the miR-34a-5p/SIRT1 axis. World J Stem Cells. 2023;15(8):842–65.
22. Liu X, Zhang Y, Zhou S, Dain L, Mei L, Zhu G. Circular RNA: an emerging frontier in RNA therapeutic targets, RNA therapeutics, and mRNA vaccines. J Control Release. 2022;348:84–94.
23. Hansen TB, Jensen TI, Clausen BH, Bramsen JB, Finsen B, Damgaard CK, Kjems J. Natural RNA circles function as efficient microRNA sponges. Nature. 2013;495(7441):384–8.
24. Li Q, Zhao YH, Xu C, Liang YL, Zhao Y, He QM, Li JY, Chen KL, Qiao H, Liu N, et al. Chemotherapy-induced senescence reprogramming promotes nasopharyngeal carcinoma metastasis by circRNA-mediated PKR activation. Adv Sci (Weinh). 2023;10(8):e2205668.
25. Zhao C, Li X, Sun G, Liu P, Kong K, Chen X, Yang F, Wang X. CircFOXO3 protects against osteoarthritis by targeting its parental gene FOXO3 and activating PI3K/AKT-mediated autophagy. Cell Death Dis. 2022;13(11):932.
26. Cheng X, Zhang L, Zhang K, Zhang G, Hu Y, Sun X, Zhao C, Li H, Li YM, Zhao J. Circular RNA VMA21 protects against intervertebral disc degeneration through targeting miR-200c and X linked inhibitor-of-apoptosis protein. Ann Rheum Dis. 2018;77(5):770–9.
27. Xie L, Huang W, Fang Z, Ding F, Zou F, Ma X, Tao J, Guo J, Xia X, Wang H, et al. CircERCC2 ameliorated intervertebral disc degeneration by regulating mitophagy and apoptosis through miR-182-5p/SIRT1 axis. Cell Death Dis. 2019;10(10):751.
28. Cherubini A, Barilani M, Rossi RL, Jalal MMK, Rusconi F, Buono G, Ragni E, Cantarella G, Simpson H, Peault B, et al. FOXP1 circular RNA sustains mesenchymal stem cell identity via microRNA inhibition. Nucleic Acids Res. 2019;47(10):5325–40.
29. Chen F, Wang S, Zeng C, Tang S, Gu H, Wang Z, Li J, Feng P, Zhang Y, Wang P, et al. Silencing circSERPINE2 restrains mesenchymal stem cell senescence via the YBX3/PCNA/p21 axis. Cell Mol Life Sci. 2023;80(11):325.
30. Pfirrmann CW, Metzdorf A, Zanetti M, Hodler J, Boos N. Magnetic resonance classification of lumbar intervertebral disc degeneration. Spine (Phila Pa 1976). 2001;26(17):1873–8.
31. Li JA-OX, Miao BA-O, Wang SA-O, Dong W, Xu H, Si C, Wang W, Duan SA-O, Lou J, Bao Z et al. Hiplot: a comprehensive and easy-to-use web service for boosting publication-ready biomedical data visualization. Brief Bioinform 2022 Jul(1477–4054 (Electronic)).
32. Liu X, Che L, Xie YK, Hu QJ, Ma CJ, Pei YJ, Wu ZG, Liu ZH, Fan LY, Wang HQ. Noncoding RNAs in human intervertebral disc degeneration: an integrated microarray study. Genom Data. 2015;5:80–1.
33. Feng J, Chen W, Dong X, Wang J, Mei X, Deng J, Yang S, Zhuo C, Huang X, Shao L, et al. CSCD2: an integrated interactional database of cancer-specific circular RNAs. Nucleic Acids Res. 2022;50(D1):D1179–83.
34. Dudekula DB, Panda AC, Grammatikakis I, De S, Abdelmohsen K, Gorospe M. CircInteractome: a web tool for exploring circular RNAs and their interacting proteins and microRNAs. RNA Biol. 2016;13(1):34–42.
35. Mon-Lopez D, Tejero-Gonzalez CM. Validity and reliability of the targetscan ISSF Pistol & Rifle application for measuring shooting performance. Scand J Med Sci Sports. 2019;29(11):1707–12.
36. Li JH, Liu S, Zhou H, Qu LH, Yang JH. starBase v2.0: decoding miRNA-ceRNA, miRNA-ncRNA and protein-RNA interaction networks from large-scale CLIP-Seq data. Nucleic Acids Res. 2014;42:D92-97.
37. Xiao F, Zuo Z, Cai G, Kang S, Gao X, Li T. miRecords: an integrated resource for microRNA-target interactions. Nucleic Acids Res. 2009;37:D105-110.
38. Rafat S, Singh P, Pandey KK, Almatroodi SA, Alsahli MA, Almatroudi A, Rahmani AH, Dev K. SMAC mimetic BV6 Co-treatment downregulates the factors involved in resistance and relapse of cancer: IAPs and autophagy. Biology (Basel). 2022;11(11):1581.
39. Fathi E, Farahzadi R. Mesenchymal stem cells as a cell-based therapeutic strategy targeting the telomerase activity of KG1 acute myeloid leukemia cells. Acta Med Iran. 2022. https://doi.org/10.18502/acta.v60i2.8817.
40. Fathi E, Azarbad S, Farahzadi R, Javanmardi S, Vietor I. Effect of rat bone marrow derived-mesenchymal stem cells on granulocyte differentiation of mononuclear cells as preclinical agent in cellbased therapy. Curr Gene Ther. 2022;22(2):152–61.
41. Wang Z, Wei D, Xiao H. Methods of cellular senescence induction using oxidative stress. Methods Mol Biol. 2013;1048:135–44.
42. Li Y, Zhuang Q, Tao L, Zheng K, Chen S, Yang Y, Feng C, Wang Z, Shi H, Shi J, et al. Urolithin B suppressed osteoclast activation and reduced bone loss of osteoporosis via inhibiting ERK/NF-kappaB pathway. Cell Prolif. 2022;55(10):e13291.
43. Troth EV, Kyle DE. EdU incorporation to assess cell proliferation and drug susceptibility in *Naegleria fowleri*. Antimicrob Agents Chemother. 2021;65(7):e0001721.
44. Debacq-Chainiaux F, Erusalimsky JD, Campisi J, Toussaint O. Protocols to detect senescence-associated beta-galactosidase (SA-betagal) activity, a biomarker of senescent cells in culture and in vivo. Nat Protoc. 2009;4(12):1798–806.
45. Rahimi P, Mobarakeh VI, Kamalzare S, SajadianFard F, Vahabpour R, Zabihollahi R. Comparison of transfection efficiency of polymer-based and lipid-based transfection reagents. Bratisl Lek Listy. 2018;119(11):701–5.
46. Bihari N. Rapid assessment of genotoxicity by flow cytometric detection of cell cycle alterations. Methods Mol Biol. 2017;1644:13–21.
47. Cossarizza A, Baccarani-Contri M, Kalashnikova G, Franceschi C. A new method for the cytofluorimetric analysis of mitochondrial membrane potential using the J-aggregate forming lipophilic cation 5,5',6,6'-tetrachloro-1,1',3,3'-tetraethylbenzimidazolcarbocyanine iodide (JC-1). Biochem Biophys Res Commun. 1993;197(1):40–5.
48. Femino AM, Fay FS, Fogarty K, Singer RH. Visualization of single RNA transcripts in situ. Science. 1998;280(5363):585–90.

49. Gagliardi M, Matarazzo MR. RIP: RNA immunoprecipitation. Methods Mol Biol. 2016;1480:73–86.
50. Alvarez ML. Faster experimental validation of microRNA targets using cold fusion cloning and a dual firefly-Renilla luciferase reporter assay. Methods Mol Biol. 2014;1182:227–43.
51. Farahzadi R, Valipour B, Anakok OF, Fathi E, Montazersaheb S. The effects of encapsulation on NK cell differentiation potency of C-kit+ hematopoietic stem cells via identifying cytokine profiles. Transpl Immunol. 2023;77:101797.
52. Vijaykumar TS, Nath A, Chauhan A. Chloroquine mediated molecular tuning of astrocytes for enhanced permissiveness to HIV infection. Virology. 2008;381(1):1–5.
53. Yue C, van der Mei HC, Kuijer R, Busscher HJ, Rochford ET. Mechanism of cell integration on biomaterial implant surfaces in the presence of bacterial contamination. J Biomed Mater Res A. 2015;103(11):3590–8.
54. Elmounedi N, Bahloul W, Turki M, Amri R, Aoui M, Elbaya W, Keskes H. Impact of needle size on the onset and the progression of disc degeneration in rats. Pain Phys. 2022;25(6):509–17.
55. Han B, Zhu K, Li FC, Xiao YX, Feng J, Shi ZL, Lin M, Wang J, Chen QX. A simple disc degeneration model induced by percutaneous needle puncture in the rat tail. Spine (Phila Pa 1976). 2008;33(18):1925–34.
56. Norcross JP, Lester GE, Weinhold P, Dahners LE. An in vivo model of degenerative disc disease. J Orthop Res. 2003;21(1):183–8.
57. Le Visage C, Kim SW, Tateno K, Sieber AN, Kostuik JP, Leong KW. Interaction of human mesenchymal stem cells with disc cells: changes in extracellular matrix biosynthesis. Spine (Phila Pa 1976). 2006;31(18):2036–42.
58. Huang Z-N, Wang Z-Y, Cheng X-F, Huang Z-Z, Han Y-L, Cui Y-Z, Liu B, Tian W. Melatonin alleviates oxidative stress-induced injury to nucleus pulposus-derived mesenchymal stem cells through activating PI3K/Akt pathway. J Orthop Transl. 2023;43:66–84.
59. Ma K, Chen S, Li Z, Deng X, Huang D, Xiong L, Shao Z. Mechanisms of endogenous repair failure during intervertebral disc degeneration. Osteoarthr Cartil. 2019;27(1):41–8.
60. Kitada T, DiAndreth B, Teague B, Weiss R. Programming gene and engineered-cell therapies with synthetic biology. Science. 2018. https://doi.org/10.1126/science.aad1067.
61. Zhang X, Jin X, Sun R, Zhang M, Lu W, Zhao M. Gene knockout in cellular immunotherapy: application and limitations. Cancer Lett. 2022;540:215736.
62. Huang Y, Zhang Z, Wang J, Shen S, Yao T, Xu Y, Chen Z, Fang B, Ma J. circSPG21 protects against intervertebral disc disease by targeting miR-1197/ATP1B3. Exp Mol Med. 2021;53(10):1547–58.
63. Xiong L, Li X, Hua X, Qian Z. Circ-STC2 promotes the ferroptosis of nucleus pulposus cells via targeting miR-486-3p/TFR2 axis. J Orthop Surg Res. 2023;18(1):518.
64. Suzuki S, Fujita N, Hosogane N, Watanabe K, Ishii K, Toyama Y, Takubo K, Horiuchi K, Miyamoto T, Nakamura M, et al. Excessive reactive oxygen species are therapeutic targets for intervertebral disc degeneration. Arthritis Res Ther. 2015;17:316.
65. Chen X, Zhang A, Zhao K, Gao H, Shi P, Chen Y, Cheng Z, Zhou W, Zhang Y. The role of oxidative stress in intervertebral disc degeneration: mechanisms and therapeutic implications. Ageing Res Rev. 2024;98:102323.
66. Wang DK, Zheng HL, Zhou WS, Duan ZW, Jiang SD, Li B, Zheng XF, Jiang LS. Mitochondrial dysfunction in oxidative stress-mediated intervertebral disc degeneration. Orthop Surg. 2022;14(8):1569–82.
67. Qian J, Ge J, Yan Q, Wu C, Yang H, Zou J. Selection of the optimal puncture needle for induction of a rat intervertebral disc degeneration model. Pain Phys. 2019;22(4):353–60.
68. Vono R, Jover Garcia E, Spinetti G, Madeddu P. Oxidative stress in mesenchymal stem cell senescence: regulation by coding and noncoding RNAs. Antioxid Redox Signal. 2018;29(9):864–79.
69. Wang F, Shi R, Cai F, Wang YT, Wu XT. Stem cell approaches to intervertebral disc regeneration: obstacles from the disc microenvironment. Stem Cells Dev. 2015;24(21):2479–95.
70. Pan X, Wu B, Fan X, Xu G, Ou C, Chen M. YAP accelerates vascular senescence via blocking autophagic flux and activating mTOR. J Cell Mol Med. 2021;25(1):170–83.
71. Zhao XP, Chang SY, Pang Y, Liao MC, Peng J, Ingelfinger JR, Chan JSD, Zhang SL. Hedgehog interacting protein activates sodium-glucose cotransporter 2 expression and promotes renal tubular epithelial cell senescence in a mouse model of type 1 diabetes. Diabetologia. 2023;66(1):223–40.
72. Lopez-Otin C, Blasco MA, Partridge L, Serrano M, Kroemer G. Hallmarks of aging: an expanding universe. Cell. 2023;186(2):243–78.
73. Guo Y, Jia X, Cui Y, Song Y, Wang S, Geng Y, Li R, Gao W, Fu D. Sirt3-mediated mitophagy regulates AGEs-induced BMSCs senescence and senile osteoporosis. Redox Biol. 2021;41:101915.
74. Zorov DB, Juhaszova M, Sollott SJ. Mitochondrial reactive oxygen species (ROS) and ROS-induced ROS release. Physiol Rev. 2014;94(3):909–50.
75. Wang J, Xia D, Lin Y, Xu W, Wu Y, Chen J, Chu J, Shen P, Weng S, Wang X, et al. Oxidative stress-induced circKIF18A downregulation impairs MCM7-mediated anti-senescence in intervertebral disc degeneration. Exp Mol Med. 2022;54(3):285–97.
76. Sun K, Jing X, Guo J, Yao X, Guo F. Mitophagy in degenerative joint diseases. Autophagy. 2021;17(9):2082–92.
77. Song Y, Liang H, Li G, Ma L, Zhu D, Zhang W, Tong B, Li S, Gao Y, Wu X, et al. The NLRX1-SLC39A7 complex orchestrates mitochondrial dynamics and mitophagy to rejuvenate intervertebral disc by modulating mitochondrial Zn(2+) trafficking. Autophagy. 2024;20(4):809–29.
78. Kang L, Liu S, Li J, Tian Y, Xue Y, Liu X. The mitochondria-targeted antioxidant MitoQ protects against intervertebral disc degeneration by ameliorating mitochondrial dysfunction and redox imbalance. Cell Prolif. 2020;53(3):12779.
79. Wang Y, Shen J, Chen Y, Liu H, Zhou H, Bai Z, Hu Z, Guo X. PINK1 protects against oxidative stress induced senescence of human nucleus pulposus cells via regulating mitophagy. Biochem Biophys Res Commun. 2018;504(2):406–14.
80. Wu ZL, Wang KP, Chen YJ, Song W, Liu Y, Zhou KS, Mao P, Ma Z, Zhang HH. Knocking down EGR1 inhibits nucleus pulposus cell senescence and mitochondrial damage through activation of PINK1-Parkin dependent mitophagy, thereby delaying intervertebral disc degeneration. Free Radic Biol Med. 2024;224:9–22.
81. Wang T, Yan X, Song D, Li Y, Li Z, Feng D. CircEYA3 aggravates intervertebral disc degeneration through the miR-196a-5p/EBF1 axis and NF-kappaB signaling. Commun Biol. 2024;7(1):390.
82. Du X, Chen S, Cui H, Huang Y, Wang J, Liu H, Li Z, Liang C, Zheng Z, Wang H. Circular RNA hsa_circ_0083756 promotes intervertebral disc degeneration by sponging miR-558 and regulating TREM1 expression. Cell Prolif. 2022;55(4):e13205.
83. Sun Y, Zhang W, Li X. Induced pluripotent stem cell-derived mesenchymal stem cells deliver exogenous miR-105-5p via small extracellular vesicles to rejuvenate senescent nucleus pulposus cells and attenuate intervertebral disc degeneration. Stem Cell Res Ther. 2021;12(1):286.
84. Zhang M, Xue X, Lou Z, Lin Y, Li Q, Huang C. Exosomes from senescent epithelial cells activate pulmonary fibroblasts via the miR-217-5p/Sirt1 axis in paraquat-induced pulmonary fibrosis. J Transl Med. 2024;22(1):310.
85. de Yebenes VG, Briones AM, Martos-Folgado I, Mur SM, Oller J, Bilal F, Gonzalez-Amor M, Mendez-Barbero N, Silla-Castro JC, Were F, et al. Aging-associated miR-217 aggravates atherosclerosis and promotes cardiovascular dysfunction. Arterioscler Thromb Vasc Biol. 2020;40(10):2408–24.
86. Menghini R, Casagrande V, Cardellini M, Martelli E, Terrinoni A, Amati F, Vasa-Nicotera M, Ippoliti A, Novelli G, Melino G, et al. MicroRNA 217 modulates endothelial cell senescence via silent information regulator 1. Circulation. 2009;120(15):1524–32.
87. Yan P, Li Z, Xiong J, Geng Z, Wei W, Zhang Y, Wu G, Zhuang T, Tian X, Liu Z, et al. LARP7 ameliorates cellular senescence and aging by allosterically enhancing SIRT1 deacetylase activity. Cell Rep. 2021;37(8):110038.
88. Ma Z, Tang P, Dong W, Lu Y, Tan B, Zhou N, Hao J, Shen J, Hu Z. SIRT1 alleviates IL-1beta induced nucleus pulposus cells pyroptosis via mitophagy in intervertebral disc degeneration. Int Immunopharmacol. 2022;107:108671.
89. Dang R, Wang M, Li X, Wang H, Liu L, Wu Q, Zhao J, Ji P, Zhong L, Licinio J, et al. Edaravone ameliorates depressive and anxiety-like behaviors via Sirt1/Nrf2/HO-1/Gpx4 pathway. J Neuroinflammation. 2022;19(1):41.

90. Ren BC, Zhang YF, Liu SS, Cheng XJ, Yang X, Cui XG, Zhao XR, Zhao H, Hao MF, Li MD, et al. Curcumin alleviates oxidative stress and inhibits apoptosis in diabetic cardiomyopathy via Sirt1-Foxo1 and PI3K-Akt signalling pathways. J Cell Mol Med. 2020;24(21):12355–67.
91. Yao ZQ, Zhang X, Zhen Y, He XY, Zhao S, Li XF, Yang B, Gao F, Guo FY, Fu L, et al. A novel small-molecule activator of Sirtuin-1 induces autophagic cell death/mitophagy as a potential therapeutic strategy in glioblastoma. Cell Death Dis. 2018;9(7):767.
92. Chen RX, Chen X, Xia LP, Zhang JX, Pan ZZ, Ma XD, Han K, Chen JW, Judde JG, Deas O, et al. N(6)-methyladenosine modification of circNSUN2 facilitates cytoplasmic export and stabilizes HMGA2 to promote colorectal liver metastasis. Nat Commun. 2019;10(1):4695.

Publisher's Note